Adjoint DSMC Method for Spatially Inhomogeneous Boltzmann Equation with General Boundary Conditions

Russel Caflisch[a], Linglai Chen[b], Yunan Yang[c,*]

[a]*Courant Institute of Mathematical Sciences, New York University, New York, NY 10012, USA*
[b]*Department of Computer Science, School of Computing, National University of Singapore, Singapore 117417, Singapore*
[c]*Department of Mathematics, Cornell University, Ithaca, NY 14853, USA*

arXiv:2603.20946v2 [math.NA] 1 Sep 2026

Abstract

We develop adjoint Direct Simulation Monte Carlo (DSMC) formulations for the spatially inhomogeneous Boltzmann equation with periodic, specular reflecting, diffuse thermal, and prescribed inflow boundary conditions. Periodic and specular boundaries are treated using a pathwise particle adjoint conditional on the realized event history. For diffuse thermal boundaries, we introduce a randomized-time regularization of wall-crossing events and use score-function terms to differentiate the resulting boundary probabilities. Reparameterization of the outgoing half-Maxwellian samples provides sensitivities with respect to wall temperatures and tangential wall velocities. Prescribed inflow requires a different construction because perturbations of incoming particles affect subsequent cell populations, local collision frequencies, and collision schedules. We therefore derive an ensemble adjoint based on the locally linearized Boltzmann collision operator and evaluate boundary sensitivities using local inflow-source scores, with injection counts held fixed. For a scalar objective, the dominant adjoint cost is largely independent of the number of parameters. Numerical experiments for Maxwell molecules validate the formulations against centered finite differences for thermal, mixed thermal-specular, two-sided inflow, and high-Mach Couette-flow configurations. The results demonstrate consistent gradient estimates, Monte Carlo convergence, stability with respect to the thermal regularization parameter, and accurate sensitivity calculation in a regime with limited relative statistical noise.

Keywords: Boltzmann equation, direct simulation Monte Carlo, DSMC, adjoint-state method, sensitivity analysis, kinetic boundary conditions.
2000 MSC: 76P05, 82C80, 65C05, 65K10, 82B40, 65M32

1. Introduction

The Boltzmann equation is a fundamental kinetic model describing the statistical behavior of dilute gases through the combined effects of particle transport and binary collisions. Numerical methods for solving the Boltzmann equation play a central role in rarefied

*Corresponding author
Email addresses: caflisch@courant.nyu.edu (Russel Caflisch), linglai_chen@u.nus.edu (Linglai Chen), yunan.yang@cornell.edu (Yunan Yang)

gas dynamics, plasma physics, radiative transfer, and related fields [10, 11]. Among these methods, Direct Simulation Monte Carlo (DSMC), originally introduced by Bird [6, 7], has emerged as a particularly flexible and robust particle-based approach. DSMC approximates the Boltzmann equation by simulating stochastic particle trajectories that alternate between particle transport, probabilistic collision events, and boundary interactions; see [19, 2, 21] for foundational analyses and algorithmic variants.

Adjoint methods are indispensable tools for sensitivity analysis, inverse problems, and partial differential equation (PDE)-constrained optimization [5, 14]. In deterministic settings, adjoint formulations for kinetic equations and their discretizations are well understood and widely used. Extending these techniques to stochastic particle methods such as DSMC is more difficult because the dependence of a realized particle trajectory on a model or boundary parameter is generally only piecewise smooth. In a spatially inhomogeneous DSMC simulation, a parameter perturbation may change the spatial cell containing a particle, the collision partners selected in that cell, whether a particle reaches a boundary during a time step, or, under an inflow boundary condition, the set of particles present in the domain. Conditional on a fixed sequence of such events, the particle updates may be differentiated pathwise away from event-switching parameter values. The derivative of this fixed realization, however, does not necessarily represent the derivative of the expected DSMC objective when the perturbation changes the probabilities or distributions associated with the discrete events. For example, under a diffuse thermal boundary condition, a small perturbation may change whether a particle reaches the wall, after which its outgoing velocity is sampled from a half-Maxwellian flux. Similar difficulties occur in adjoint Monte Carlo methods for radiative transfer, neutron transport, and stochastic chemical kinetics [15, 3, 24].

Adjoint and gradient-based methods for kinetic equations have attracted growing interest in optimization, control, and inverse problems [18, 17]. For radiative transport and kinetic models, Monte Carlo gradient and adjoint formulations have clarified when pathwise differentiation is valid and when likelihood-ratio or score-function corrections are required to account for parameter-dependent sampling and discrete event selection [16, 25, 20]. In the context of the Boltzmann equation, adjoint DSMC formulations have been derived for spatially homogeneous problems with general collision models [8, 25], and broader perspectives on adjoint Monte Carlo methods for kinetic equations are provided in [9]. Parallel developments in adjoint-based optimization for rarefied gas flows have employed deterministic kinetic solvers, including discrete-velocity and BGK-type methods, to enable topology and shape optimization across rarefied and continuum regimes [13, 26, 27].

Automatic differentiation (AD) computes derivatives of numerical programs by applying the chain rule, either in forward mode using dual numbers or in reverse mode through a computational graph [12, 4, 23]. However, black-box AD applied to a realized DSMC trajectory treats discrete choices, such as cell assignments, collision-pair selections, boundary events, and parameter-dependent sampling laws, as fixed. It therefore does not generally recover the derivative of the expected DSMC objective when a parameter changes the probabilities of these events. This limitation motivates the specialized pathwise, score-function, and ensemble-adjoint formulations developed here.

The present work develops complementary adjoint DSMC formulations for the spatially inhomogeneous Boltzmann equation with periodic, specular reflecting, diffuse thermal, and prescribed inflow boundary conditions. For periodic and specular boundaries, we employ a

pathwise discrete adjoint that differentiates the realized particle updates while holding the sampled random variables and the associated discrete event history fixed. Away from spatial-cell and boundary interfaces, the hard cell-membership indicators are locally constant, and their derivatives therefore vanish almost surely along the realized trajectory. The resulting adjoint propagates sensitivities with respect to both the initial velocity distribution and the initial spatial distribution.

Diffuse thermal boundaries require additional treatment because a parameter perturbation may switch the boundary hit-or-miss event. We introduce a selective randomized-time regularization for particles that may interact with a thermal wall. For a fixed regularization width ε, the resulting adjoint computes the derivative of an ε-regularized objective J_ε. Score-function terms capture the sensitivity of the boundary-crossing probabilities, while reparameterizations of the half-Maxwellian flux yield derivatives with respect to wall temperatures and prescribed tangential wall velocities. The regularized scheme converges to the original DSMC update as $\varepsilon \to 0$, and the numerical experiments examine the stability of both the objective and the adjoint gradient over the range of ε used in the calculations.

Prescribed inflow boundaries require a different formulation. A perturbation of an incoming-particle distribution changes not only the injected particle states but also their subsequent cell memberships, the local particle densities, and the collision schedules. A pathwise adjoint that freezes one realized sequence of cell memberships and collision pairs therefore does not, in general, recover the derivative of the expected DSMC objective. We instead differentiate the ensemble evolution and obtain a scalar backward equation involving the adjoint of the locally linearized Boltzmann collision operator. This construction extends the continuous linearized-collision framework of our earlier work [8] to a spatially inhomogeneous setting and couples it to free transport, absorbing outflow, and parameter-dependent boundary sources. The derivative of each inflow source is evaluated using a local likelihood-ratio score of the incoming flux distribution. A Monte Carlo discretization that retains a prescribed subset of particle states in each cell limits the storage required by the backward calculation. For a scalar objective, the dominant forward and backward costs are largely independent of the number of inflow parameters.

The proposed formulations are examined in four numerical examples. The first two examples consider two-sided thermal boundaries and mixed thermal-specular boundaries, respectively, and include sensitivities with respect to boundary temperatures and parameters in the initial velocity and spatial distributions. The third example validates the ensemble-adjoint formulation for a two-sided inflow problem and studies its dependence on the number of retained particle states. The fourth example considers a high-Mach-number planar Couette flow driven by moving thermal walls. It tests the wall-speed derivative in a regime where the sensitivity signal is clearly resolved relative to the statistical fluctuations. In all cases, the adjoint estimates are compared with centered finite-difference estimates using common random numbers.

The remainder of the paper is organized as follows: Section 2 reviews background on the Boltzmann equation and the forward and adjoint DSMC algorithms. Section 3 derives adjoint equations for DSMC with periodic and specular reflecting boundary conditions. Section 4 develops the adjoint formulation for thermal boundary conditions using randomized time stepping. Section 5 introduces the ensemble-adjoint formulation and the local boundary-source score for prescribed inflow conditions. Several numerical examples are presented in

Section 6. We conclude in Section 8 with a discussion of implications for adjoint particle methods for transport-dominated PDEs.

2. Background

In this section, we briefly review the essential background for the spatially inhomogeneous Boltzmann equation with the bilinear collision operator, the DSMC method, and the adjoint DSMC method proposed in [8, 25, 9].

We adopt the argument order $f(x, v, t)$ for the distribution function, and $r(x, v)$ for observables. The projection $\mathcal{P}$ maps velocities to spatial dimensions (e.g., $\mathcal{P} = e_1^\top$ in 1D). Primes denote post-collision quantities, and $(v_{k,i}, x_{k,i})$ denotes the ith particle state at time t_k. Adjoint variables associated with $(v_{k,i}, x_{k,i})$ are $(\beta_{k,i}, \alpha_{k,i})$.

We remark that the adjoint variables introduced throughout this work are mathematically equivalent to Lagrange multipliers in constrained optimization. In this setting, the adjoint variable enforces the kinetic evolution equation and enables efficient computation of gradients of objective functionals with respect to parameters. Thus, adjoint variables serve the same fundamental purpose as Lagrange multipliers by encoding sensitivity of the objective to constraints.

2.1. Boltzmann Equation

We consider the spatially inhomogeneous Boltzmann equation on a finite spatial domain Ω,

$$\frac{\partial f}{\partial t} + v \cdot \nabla_x f = Q(f, f), \tag{1}$$

subject to the initial condition

$$f(x, v, 0) = f_0(x, v), \tag{2}$$

and appropriate boundary conditions (BCs) prescribed on $\partial\Omega$, which will be specified in Sections 3 to 5. Here, $f(x, v, t)$ is a nonnegative density function describing the time evolution of particles located at position $x \in \Omega$ with velocity $v \in \mathbb{R}^3$ at time $t > 0$.

The bilinear collision operator $Q(f, f)$ models binary particle collisions and is given by

$$Q(f, f) = \int_{\mathbb{R}^3} \int_{\mathbb{S}^2} q(v - v_1, \sigma)\big(f(v_1')f(v') - f(v_1)f(v)\big)\, d\sigma\, dv_1, \tag{3}$$

where (v', v_1') denote the post-collisional velocities corresponding to the pre-collisional velocities (v, v_1), and the integration in σ is taken over the unit sphere $\mathbb{S}^2$. Note that $Q(f, f)$ and f in (3) are functions of the spatial variable x, velocity variable v and time variable t.

In this work, we focus on the effects arising from spatial transport and BCs. Accordingly, for simplicity we restrict attention to Maxwell molecules, for which the collision kernel $q(v - v_1, \sigma)$ is constant. The proposed adjoint formulation, however, extends directly to more general collision kernels; see [25].

Because of conservation of the momentum $v + v_1$ and the energy $v^2 + v_1^2$, the elastic collision formulae satisfy

$$v' = 1/2(v + v_1) + 1/2|v - v_1|\sigma, \tag{4}$$

$$v_1' = 1/2(v + v_1) - 1/2|v - v_1|\sigma, \tag{5}$$

where σ is a collision parameter representing a unit direction of the relative velocity of particles after collision. We will hereafter use the shorthand notation f, f_1, f', f_1' to denote $f(v), f(v_1), f(v')$ and $f(v_1')$. Let

$$\zeta = (v - v_1)\hat{}, \quad \sigma = (v' - v_1')\hat{}, \tag{6}$$

where the notation $x\hat{} = x/|x|$. The collision rules (4) and (5) can be presented in an operator formulation as

$$\begin{bmatrix} v' \\ v_1' \end{bmatrix} = A(\sigma, \zeta) \begin{bmatrix} v \\ v_1 \end{bmatrix}, \quad \begin{bmatrix} v \\ v_1 \end{bmatrix} = B(\sigma, \zeta) \begin{bmatrix} v' \\ v_1' \end{bmatrix}, \tag{7}$$

where

$$A(\sigma, \zeta) = \frac{1}{2} \begin{bmatrix} I + \sigma\zeta^\top & I - \sigma\zeta^\top \\ I - \sigma\zeta^\top & I + \sigma\zeta^\top \end{bmatrix}, \quad B(\sigma, \zeta) = \frac{1}{2} \begin{bmatrix} I + \zeta\sigma^\top & I - \zeta\sigma^\top \\ I - \zeta\sigma^\top & I + \zeta\sigma^\top \end{bmatrix}, \tag{8}$$

where I is the identity matrix in $\mathbb{R}^3$ and $B = A^\top = A^{-1}$. It was shown in [8] that for Maxwell molecules, the first-order variations (with collision parameters fixed) in pre- and post-collision velocities satisfy

$$\begin{bmatrix} \delta v' \\ \delta v_1' \end{bmatrix} = A(\sigma, \zeta) \begin{bmatrix} \delta v \\ \delta v_1 \end{bmatrix}. \tag{9}$$

Note that when the collision parameters (i.e., σ and ζ) are fixed, (7) defines a linear operation, namely a matrix-vector product.

2.2. The DSMC Method

In this section, we describe the classical Direct Simulation Monte Carlo (DSMC) method [6, 19, 2, 1] for the spatially inhomogeneous Boltzmann equation (1), following the tutorial presentation in [21]. A standard approach for treating spatial inhomogeneity is operator splitting, which separates the collision dynamics from the advection (transport) dynamics. Specifically, one first solves the spatially homogeneous Boltzmann equation

$$\frac{\partial f}{\partial t} = Q(f, f) \tag{10}$$

over a single time step, using the initial condition (2). The resulting solution is then used as the initial condition for the transport equation

$$\frac{\partial f}{\partial t} + v \cdot \nabla_x f = 0, \tag{11}$$

which is likewise solved over one time step. The composition of these two substeps yields an approximation to the solution of the full Boltzmann equation (1) after one time step, and the procedure is iterated in time.

The DSMC method for (1) is also based on such an operator splitting. We consider a collection of N Monte Carlo particles evolving over the time interval $[0, T]$. The interval is divided into M subintervals of equal length $\Delta t = T/M$. At the kth time level $t_k = k\Delta t$, the particle velocities are given by

$$\mathcal{V}_k = \{v_1, \ldots, v_N\}(t_k), \tag{12}$$

Algorithm 1 Nanbu–Babovsky Algorithm for Maxwell Molecules

Sample the initial particle velocities and positions, given the initial particle density $f_0(x, v)$, to get $\mathcal{V}_0 = \{v_{0,1}, \ldots, v_{0,N}\}$ and $\mathcal{X}_0 = \{x_{0,1}, \ldots, x_{0,N}\}$. Set $M = T/\Delta t$ for final time T. Divide the spatial domain Ω into N_c spatial cells: $\Omega = \Omega_1 \cup \ldots \cup \Omega_{N_c}$.
for $k = 1$ to M **do**
    Given the set of particle velocities $\mathcal{V}_{k-1}$ and positions $\mathcal{X}_{k-1}$ from time step t_{k-1}.
    for $j = 1$ to N_c **do**
        Identify $\mathcal{V}_{k-1}^j \subseteq \mathcal{V}_{k-1}$ where the particle positions are in the j-th spatial cell Ω_j.
        Let $N_{k-1}^j = |\mathcal{V}_{k-1}^j|$ and define the local density and collision frequency by $\rho_{k-1}^j = N_{k-1}^j/(N|\Omega_j|)$ and $\mu_{k-1}^j = \rho_{k-1}^j \int_{\mathbb{S}^2} q(\sigma)\, d\sigma$. Select $\lceil N_{k-1}^j \Delta t\, \mu_{k-1}^j/2 \rceil$ collision pairs uniformly without replacement from $\mathcal{V}_{k-1}^j$.
        For each selected pair $(v_{k-1,i}, v_{k-1,i_1})$, perform collision based on (4)-(5); obtain post-collision velocities $(v'_{k-1,i}, v'_{k-1,i_1})$. Set $v'_{k-1,i} = v_{k-1,i}$ for particles that do not collide.
    end for
    Compute the new spatial position $x'_{k-1,i}$ based on (14).
    if $x'_{k-1,i} \in \Omega$ **then**
        Set $v_{k,i} = v'_{k-1,i}$ and $x_{k,i} = x'_{k-1,i}$.
    else
        Enforce the specific boundary conditions and obtain $v_{k,i}$ and $x_{k,i}$.
    end if
end for

where we denote the velocity of the ith particle by $v_i(t_k)$ or equivalently $v_{k,i}$. Each particle is also associated with a spatial position

$$\mathcal{X}_k = \{x_1, \ldots, x_N\}(t_k), \tag{13}$$

with $x_{k,i}$ denoting the position of the ith particle at time t_k. We assume that all particles lie within the spatial domain Ω at the initial time $t = 0$.

As in [8], we focus on a Maxwellian gas with a constant collision kernel, i.e., $q(v - v_1, \sigma) = C$. The algorithm described in this subsection can, however, be extended to more general collision kernels; see, for example, [6, 21]. A summary of the DSMC algorithm is provided in Algorithm 1. In contrast to the spatially homogeneous setting, each collision step is followed by an advection step.

According to (11), the post-collision spatial position of each particle is updated as

$$x'_{k,i} = x_{k,i} + \Delta t\, \mathcal{P} v'_{k,i}, \tag{14}$$

where $\mathcal{P}$ denotes a projection operator mapping velocities in $\mathbb{R}^3$ to the spatial domain. For example, if $\Omega \subset \mathbb{R}$, then $\mathcal{P} = \mathbf{e}_1^\top = [1, 0, 0]$; for a two-dimensional spatial domain, $\mathcal{P} = [\mathbf{e}_1, \mathbf{e}_2]^\top$; and for a three-dimensional spatial domain, $\mathcal{P}$ is the identity matrix. Following this update, particle positions are required to remain within the spatial domain Ω through the enforcement of appropriate BCs.

While the spatial domain Ω may be one-, two-, or three-dimensional, the velocity space is always taken to be the full $\mathbb{R}^3$. Viewed in this way, Algorithm 1 implements DSMC for

the homogeneous Boltzmann equation (10), followed by the advection step (14) and the enforcement of BCs on the spatial domain.

Finally, we note that under inflow BCs, the total number of Monte Carlo particles N may vary in time, whereas for the other BCs considered in this work, including periodic boundaries, specular reflection, and thermalization, the particle number remains constant.

2.3. The Adjoint DSMC Method

The adjoint DSMC method was first proposed in [8] as an efficient particle-based method to compute the gradient for Boltzmann-equation constrained optimization problems for Maxwell molecules. It was later generalized to adapt to more general collision kernels, such as the variable hard sphere models [25]. The idea of using adjoint Monte Carlo-type methods for kinetic equation-constrained optimization is more general and applies to the radiative transport equation [16]. We refer interested readers to [9] for a survey.

For the Boltzmann equation with a constant collision kernel, the pathwise adjoint used for periodic, specular, and thermal boundary conditions can be interpreted as the formal adjoint of the forward DSMC method in Algorithm 1, conditional on the random variables and discrete event history sampled during the forward simulation. Adjoint DSMC methods were previously developed for the spatially homogeneous Boltzmann equation (10). The present work extends this framework to spatial transport and several boundary conditions. The prescribed-inflow problem requires a different ensemble-adjoint formulation, developed in Section 5, because freezing the realized cell memberships and collision schedule does not generally capture the derivative of the expected inflow objective.

Consider a simple optimization problem for the spatially homogeneous Boltzmann equation (10). The initial condition is

$$f(v,0) = f_0(v;m), \tag{15}$$

in which f_0 is the prescribed initial data depending on a parameter m. The goal is to find m which optimizes the objective function at time $t = T$,

$$J_1(m) = \int_{\mathbb{R}^3} r(v) f(v,T) dv, \tag{16}$$

where $f(v,T)$ is the solution to (10) given the initial condition (15), and thus $f(v,T)$ depends on m through the initial condition. Here, we take parameters in the initial distribution as an illustrative example of the optimization problem, but the proposed approach readily extends to other types of parameters appearing in the Boltzmann equation; the same applies to the choice of objective function (16).

To compute the gradient of J_1 with respect to a parameter m, [8] considered the following total objective function $\mathcal{J}$ (i.e., Lagrangian) with Lagrangian multipliers $\{\beta_{k,i}\}$:

$$\mathcal{J} = \underbrace{\frac{1}{N}\sum_{i=1}^{N} r(v_{M,i})}_{\mathcal{J}_1} + \underbrace{\frac{1}{N}\sum_{i=1}^{N} \beta_{0,i}\cdot(v_{0,i} - v_{0,i}(m))}_{\mathcal{J}_2} + \underbrace{\frac{1}{N}\sum_{k=0}^{M-1}\sum_{i=1}^{N} \beta_{k,i}\cdot(v_{k+1,i} - v'_{k,i})}_{\mathcal{J}_3}. \tag{17}$$

Here, $\mathcal{J}_1$ is the Monte Carlo quadrature of the objective function (16) by particle velocities $\{v_{M,i}\}_{i=1}^N$ at the final time, $\mathcal{J}_2$ is the constraint on the DSMC initial condition $v = v_0(m)$

using the adjoint variable $\{\beta_{0,i}\}_{i=1}^N$, and $\mathcal{J}_3$ is the constraint that enforces the binary collision law (4) and (5) using the adjoint variable $\beta_{k,i}$ for each particle i at the kth time interval. In particular, $v'_{k,i}$ represents the post-collision velocity of particle i if it participates in a collision at the kth time interval. Otherwise, $v'_{k,i} = v_{k,i}$, which means the particle velocity remains the same at the $(k+1)$th time interval. The advantage of the Lagrangian approach is that $\{v_{k,i}\}$ is a general set of velocities, and its dependence on the collision rules (4)-(5) is imposed through the adjoint variables.

By setting the derivatives of $\mathcal{J}$ with respect to the adjoint variables $\{\beta_{k,i}\}$ as zero, we get the collision rule (4)-(5) and the initial condition (15). By setting the derivatives of $\mathcal{J}$ with respect to the state variables $\{v_{k,i}\}$, we get the adjoint equations, which can be rewritten using the operator notation (8):

$$\begin{bmatrix} \beta_{k,i} \\ \tilde{\beta}_{k,i_1} \end{bmatrix} = C \begin{bmatrix} \beta_{k+1,i} \\ \tilde{\beta}_{k+1,i_1} \end{bmatrix}, \quad C = \begin{cases} B(\sigma_{k,i}, \zeta_{k,i}), & \text{if } (v_{k,i}, v_{k,i_1}) \text{ collided at } t_k, \\ I, & \text{otherwise,} \end{cases} \tag{18}$$

in which $\zeta_{k,i} = (v_{k,i} - v_{k,i_1})\hat{}$, $\sigma_{k,i}$ is the collision parameter for the pair, and $I \in \mathbb{R}^{6\times 6}$ is the identity matrix. The adjoint equation evolves backward in time with a given final condition

$$\beta_{M,i} = -\nabla_v r(v_{M,i}), \quad 1 \le i \le N. \tag{19}$$

The gradient of the objective function with respect to the parameter m is

$$\partial_m \mathcal{J} = -\frac{1}{N} \sum_{i=1}^{N} \beta_{0,i} \cdot \partial_m v_{0,i}(m),$$

which can be computed using the adjoint variables $\{\beta_{0,i}\}$. They are solved backward in time following (18) with the final condition (19).

For more general optimization problems involving the Boltzmann equation, that are different from (15) and (16), this procedure can be directly followed to obtain a more general version of the total objective function (17), which can then be optimized as above.

The adjoint DSMC method enables efficient computation of gradients for Boltzmann-constrained optimization problems at a cost that is largely independent of the number of optimization parameters, making it particularly well suited for high-dimensional and stochastic settings. Moreover, adjoint variable backpropagation closely mirrors the structure of the forward DSMC simulation, allowing gradient information to be propagated backward along particle trajectories using the same random samples generated in the forward run, thereby avoiding additional sampling and incurring only minimal computational overhead.

3. Adjoint DSMC Method With Periodic and Specular Reflecting Boundary Conditions

The adjoint DSMC method reviewed in Section 2.3 is based on the spatially homogeneous Boltzmann equation (10), as developed in [8]. We now extend this framework to the spatially inhomogeneous Boltzmann equation (1).

To illustrate the methodology, we first consider a simple Boltzmann-constrained optimization problem associated with (1). The initial condition is given by

$$f(x, v, 0) = f_0(x, v; m), \tag{20}$$

where f_0 is prescribed initial data depending on the parameter m. For a general parameterized initial distribution, the initial particles may be generated from parameter-independent random seeds through a deterministic differentiable sampling map Ψ:

$$(x_{0,i}, v_{0,i}) = \Psi(\xi_i; m),$$

where ξ_i is a random variable whose distribution does not depend on m. In what follows, we write $x_{0,i} = x_{0,i}(m)$ and $v_{0,i} = v_{0,i}(m)$ to emphasize the dependence of the initial samples on the parameter.

The objective is to determine parameters m that optimize a terminal-time functional of the form

$$J_1(m) = \int_\Omega \int_{\mathbb{R}^3} r(x, v)\, f(x, v, T)\, dv\, dx, \tag{21}$$

where $f(x, v, T)$ denotes the solution of (1) at time $t = T$ corresponding to the initial condition (20). The terminal distribution $f(x, v, T)$ depends on the parameter m through the initial condition.

As before, the specific choices of parameterization and objective function are purely illustrative, and the proposed adjoint DSMC framework applies to more general parameterizations and objective functions.

Using adjoint variables, we define

$$\mathcal{J}_1 = \frac{1}{N} \sum_{i=1}^{N} r(v_{M,i}, x_{M,i}), \tag{22}$$

$$\mathcal{J}_2 = \frac{1}{N} \sum_{i=1}^{N} \beta_{0,i} \cdot \big(v_{0,i} - v_{0,i}(m)\big) + \frac{1}{N} \sum_{i=1}^{N} \alpha_{0,i} \cdot \big(x_{0,i} - x_{0,i}(m)\big), \tag{23}$$

$$\mathcal{J}_3 = \frac{1}{N} \sum_{k=0}^{M-1} \sum_{i \in N_{\text{in}}^k} \beta_{k+1,i} \cdot \big(v_{k+1,i} - v'_{k,i}\big) + \frac{1}{N} \sum_{k=0}^{M-1} \sum_{i \in N_{\text{in}}^k} \alpha_{k+1,i} \cdot \big(x_{k+1,i} - x'_{k,i}\big), \tag{24}$$

where

$$N_{\text{in}}^k = \{i \in \{1, \ldots, N\} : x'_{k,i} \in \Omega\}$$

denotes the set of particle indices whose post-collision positions remain inside the domain Ω, and $v'_{k,i}$ denotes the post-collision velocity associated with $v_{k,i}$. We denote $\beta_{k,i}$ as the adjoint variable corresponding to the particle velocity $v_{k,i}$ and $\alpha_{k,i}$ as the adjoint variable corresponding to the particle position $x_{k,i}$, for $i = 1, \ldots, N$ and $k = 0, \ldots, M$.

Here, $\mathcal{J}_1$ represents the Monte Carlo approximation of the objective function (21) at the final time, where $r(x, v)$ denotes the observable. The terms in $\mathcal{J}_2$ enforce the constraints on the initial particle velocities and positions through the adjoint variables $\{\beta_{0,i}\}$ and $\{\alpha_{0,i}\}$, respectively, with the joint initial samples $(x_{0,i}(m), v_{0,i}(m)) = \Psi(\xi_i; m)$ generated by the

general sampling map introduced above; no independence between the initial position and velocity is required. The terms in $\mathcal{J}_3$ impose the collision and advection constraints using the adjoint variables $\{\beta_{k,i}\}$ and $\{\alpha_{k,i}\}$ for particles that remain inside the domain after the update ($x'_{k,i} \in \Omega$). For particles that exit the domain, BCs are applied, and the corresponding particle variables $\{v_{k,i}\}$ and $\{x_{k,i}\}$ are no longer subject to the constraints in $\mathcal{J}_3$.

We conclude this subsection with a few remarks on notation that will appear repeatedly. In the forward DSMC algorithm (Algorithm 1), at each time step t_k particles are grouped into pairs $(v_{k,i}, v_{k,i_1})$, where i_1 denotes the pairing index of particle i at time t_k. Depending on the collision kernel, a subset of these pairs is selected to undergo collisions.

- If the pair $(v_{k,i}, v_{k,i_1})$ is selected for collision in the forward DSMC process at time t_k, one would sample the parameter $\sigma_{k,i}$, the post-collision relative velocity direction, and compute $\zeta_{k,i}$, the pre-collision relative velocity. In this case, we use the 6×6 matrix $B(\sigma_{k,i}, \zeta_{k,i})$ defined in (8) in the adjoint equations.
- If the pair $(v_{k,i}, v_{k,i_1})$ is *not* selected for collision, we slightly abuse notation and set $B_{k,i} = I$, where I denotes the 6×6 identity matrix.

Combining both cases, we define the operator $B_{k,i}$ by

$$B_{k,i} = \begin{cases} B(\sigma_{k,i}, \zeta_{k,i}), & \text{if } (v_{k,i}, v_{k,i_1}) \text{ collides at time } t_k, \\ I, & \text{otherwise.} \end{cases} \tag{25}$$

An important observation is that $B_{k,i} = B_{k,i_1}$.

Next, we discuss periodic and specular reflection BCs. Additional Lagrangian terms associated with these BCs must be introduced.

3.1. Periodic Boundary Condition

We begin by considering a 1D spatial domain $\Omega = [L, R] \subset \mathbb{R}$. The periodic BC enforces the following update whenever $x'_{k,i} \notin \Omega$:

$$x_{k+1,i} = L + \big(x'_{k,i} \bmod (R - L)\big), \tag{26}$$

where $a \bmod b$ denotes the smallest nonnegative real number c such that $(a - c)/b$ is an integer. Under periodic BCs, the particle velocity is unchanged by boundary crossing, i.e., $v_{k+1,i} = v'_{k,i}$ regardless of whether $x'_{k,i}$ lies inside Ω. The above formulation readily extends to periodic BCs on more general spatial domains in $\mathbb{R}^d$.

For simplicity, we present the derivation in the 1D setting $\Omega = [L, R]$. In this case, the functional $\mathcal{J}_3$ in (24) is replaced by the following expression, which incorporates the periodic BC:

$$\begin{aligned} \mathcal{J}_3^{p1} \;=\; & \frac{1}{N} \sum_{k=0}^{M-1} \sum_{i=1}^{N} \beta_{k+1,i} \cdot \big(v_{k+1,i} - v'_{k,i}\big) \\ & + \frac{1}{N} \sum_{k=0}^{M-1} \sum_{i=1}^{N} \alpha_{k+1,i} \Big(x_{k+1,i} - \Big(L + (x'_{k,i} \bmod (R - L)) \Big) \Big). \end{aligned} \tag{27}$$

We consider the unconstrained optimization problem defined by the augmented objective

$$\mathcal{J} = \mathcal{J}_1 + \mathcal{J}_2 + \mathcal{J}_3^{p1},$$

where $\mathcal{J}_1$ and $\mathcal{J}_2$ are given by (22)-(23). The superscript $p1$ indicates the 1D periodic setting.

The initial condition, collision rule, advection rule, and BC are recovered by differentiating $\mathcal{J}$ with respect to the adjoint variables

$$\{\beta_{k,i}\}, \quad \{\alpha_{k,i}\}, \qquad k = 0, \ldots, M, \quad i = 1, \ldots, N.$$

The adjoint equations are then obtained by setting the derivatives of $\mathcal{J}$ with respect to all state variables $\{v_{k,i}\}$ and $\{x_{k,i}\}$ to zero.

For any spatial dimension $d = 1, 2, 3$, the terminal conditions for the adjoint variables $\beta_{M,i}$ and $\alpha_{M,i}$, $i = 1, \ldots, N$, are given by

$$\begin{aligned} \beta_{M,i} &= -\partial_v r(x_{M,i}, v_{M,i}), && (28) \\ \alpha_{M,i} &= -\partial_x r(x_{M,i}, v_{M,i}). && (29) \end{aligned}$$

The adjoint variables $\{\beta_{k,i}\}$ and $\{\alpha_{k,i}\}$ are then propagated backward in time for $k = 0, \ldots, M-1$ according to

$$\begin{aligned} \begin{bmatrix} \beta_{k,i} \\ \beta_{k,i_1} \end{bmatrix} &= B_{k,i} \begin{bmatrix} \beta_{k+1,i} + \Delta t\, \mathcal{P}^* \alpha_{k+1,i} \\ \beta_{k+1,i_1} + \Delta t\, \mathcal{P}^* \alpha_{k+1,i_1} \end{bmatrix}, \quad \text{for all collision pairs } (i, i_1), && (30) \\ \alpha_{k,i} &= \alpha_{k+1,i}, \quad \text{for all } i = 1, \ldots, N, && (31) \end{aligned}$$

where $B_{k,i}$ is defined in (25). The adjoint projection operator $\mathcal{P}^*$ is given by $\mathcal{P}^* = \mathbf{e}_1$ in one dimension, $\mathcal{P}^* = [\mathbf{e}_1, \mathbf{e}_2]$ in two dimensions, and $\mathcal{P}^* = I$ in three dimensions.

Once the adjoint variables $\{\beta_{0,i}\}$ and $\{\alpha_{0,i}\}$ at the initial time $t = 0$ have been computed, the gradient of the objective function with respect to the parameters in the initial velocity and spatial distributions can be evaluated as

$$\partial_m \mathcal{J} = -\frac{1}{N} \sum_{i=1}^{N} \left[\beta_{0,i} \cdot \nabla_m v_{0,i}(m) + \alpha_{0,i} \cdot \nabla_m x_{0,i}(m) \right]. \tag{32}$$

3.2. Reflecting Boundary Condition

Next, we consider the specular (mirror) reflection boundary condition, in which a particle undergoes mirror reflection upon reaching the boundary of the spatial domain Ω.

Let (v^*, x^*) denote the velocity and spatial position of a particle with $x^* \notin \Omega$. For the moment, we assume that v^* and x^* have the same dimension. Let $\mathbf{n}$ denote the outward unit normal vector at the boundary. The hyperplane defining the spatial reflection is given by $\{x \cdot \mathbf{n} = c\}$ for a constant c determined by the boundary, while the corresponding hyperplane for velocity reflection is $\{v \cdot \mathbf{n} = 0\}$. The reflected particle has velocity v and position x given by

$$\begin{aligned} v &= v^* - 2\mathbf{n}(\mathbf{n} \cdot v^*), \\ x &= x^* - 2\mathbf{n}(\mathbf{n} \cdot x^* - c). \end{aligned}$$

Throughout, we neglect the possibility that a particle with sufficiently large velocity may cross the boundary more than once during a single time step, but this is easily included in the algorithm.

We now specialize to the setting in which the velocity domain is $\mathbb{R}^3$, while the spatial domain Ω is a subset of $\mathbb{R}$, $\mathbb{R}^2$, or $\mathbb{R}^3$. For clarity, we present the derivation in the 1D case and then state the final adjoint equations in full generality.

Consider the 1D spatial domain $\Omega = [L, R] \subset \mathbb{R}$, with $v^* \in \mathbb{R}^3$ and $x^* \in \mathbb{R}$. If $x^* \notin \Omega$, the reflecting BC takes the form

$$\begin{aligned} x &= b - |x^* - b| \operatorname{sgn}(v^* \cdot \mathbf{e}_1) = 2b - x^*, \\ v &= [v_x, v_y, v_z]^\top = [-v_x^*,\, v_y^*,\, v_z^*]^\top, \end{aligned}$$

where $b = L$ if $x^* < L$ and $b = R$ if $x^* > R$. Here, $\mathbf{e}_1 = [1, 0, 0]^\top$, and $\operatorname{sgn}(\cdot)$ is the sign function.

To enforce the reflecting BC within the adjoint formulation, we modify the Lagrangian to incorporate additional constraints beyond those in (22)-(23). For each time step t_k, the post-collision positions $x'_{k,i}$ are partitioned into three disjoint sets: N^k_{in}, consisting of particles with $x'_{k,i} \in [L, R]$; $N^k_{\text{out}_L}$, consisting of particles with $x'_{k,i} < L$; and $N^k_{\text{out}_R}$, consisting of particles with $x'_{k,i} > R$. We replace (24) by

$$\begin{aligned} \mathcal{J}_3^{r1} &= \frac{1}{N} \sum_{k=0}^{M-1} \sum_{i=1}^{N} \beta_{k+1,i} \cdot \left(v_{k+1,i} - C_{k,i} v'_{k,i}\right) \\ &\quad + \frac{1}{N} \sum_{k=0}^{M-1} \sum_{i=1}^{N} \alpha_{k+1,i} \Big(x_{k+1,i} - \mathbb{1}_{i \in N^k_{\text{out}_L}} (2L - x'_{k,i}) - \mathbb{1}_{i \in N^k_{\text{out}_R}} (2R - x'_{k,i}) - \mathbb{1}_{i \in N^k_{\text{in}}} x'_{k,i} \Big), \end{aligned}$$

where the diagonal matrix

$$C_{k,i} = \operatorname{diag}\Big([\, 2\, \mathbb{1}_{i \in N^k_{\text{in}}} - 1,\ 1,\ 1\,] \Big) \tag{33}$$

enforces the velocity reflection in the normal direction.

The full objective function is then given by

$$\mathcal{J} = \mathcal{J}_1 + \mathcal{J}_2 + \mathcal{J}_3^{r1}.$$

Proceeding as in Section 3.1, the adjoint equations are obtained by setting the derivatives of $\mathcal{J}$ with respect to all state variables equal to zero.

When the spatial domain is a connected interval (1D), a rectangle (2D), or a cuboid (3D), the resulting adjoint equations simplify as follows. The terminal conditions for the adjoint variables remain identical to (28) and (29). For each particle index $i = 1, \ldots, N$ and time step $k = 0, \ldots, M-1$, the adjoint variables satisfy

$$\begin{bmatrix} \beta_{k,i} \\ \beta_{k,i_1} \end{bmatrix} = B_{k,i} \begin{bmatrix} C_{k,i}\big(\beta_{k+1,i} + \Delta t\, \mathcal{P}^* \alpha_{k+1,i}\big) \\ C_{k,i_1}\big(\beta_{k+1,i_1} + \Delta t\, \mathcal{P}^* \alpha_{k+1,i_1}\big) \end{bmatrix}, \quad \text{for all collision pairs } (i, i_1), \tag{34}$$

$$\mathcal{P}^* \alpha_{k,i} = C_{k,i}\, \mathcal{P}^* \alpha_{k+1,i}, \quad \text{for all } i = 1, \ldots, N, \tag{35}$$

where $B_{k,i}$ is defined in (25), the adjoint projection operator $\mathcal{P}^*$ is defined dimension-wise as in Section 3.1, and the matrix $C_{k,i}$ depends on the spatial dimension according to (33).

Finally, once the adjoint variables have been fully back-propagated, the gradients with respect to the parameter m are computed using (32).

4. Adjoint DSMC Method With Thermal Boundary Conditions

In Section 3, we discussed strategies for handling periodic and specular (mirror) reflecting BCs. Here, we focus on the thermal BC, which is more complex than the previous cases and requires a slight modification of the forward DSMC algorithm. Note that different BCs for the forward DSMC algorithm only affect Line 13 of Algorithm 1.

For the thermal BC, a particle that hits the boundary is absorbed and then re-emitted into the domain with a velocity randomly drawn from the thermal equilibrium flux at the wall, which is given by a half-Maxwellian distribution [21]. Given an outward unit normal vector n, the reflected velocity v is sampled from a half-Maxwellian flux satisfying $v \cdot n < 0$.

We next describe the Boltzmann equation with thermal BCs for the 1D spatial domain $\Omega = [L, R]$. The thermal BC is enforced whenever the post-collision spatial position $x'_{k,i}$ satisfies either $x'_{k,i} < L$ or $x'_{k,i} > R$. In this case, the original velocity is replaced by a sample from the half-Maxwellian flux with temperature parameter T_L (for the left boundary) or T_R (for the right boundary), respectively, and the spatial position is determined by the thermal BC rule [21, Alg. 6.3]:

- If $x'_{k,i} < L$, we sample $g_{k,i} \in \mathbb{R}^3$ from the half-Maxwellian flux $-v \cdot n_L \, M_{T_L}(v) \, \mathbb{1}_{v \cdot n_L < 0}$ (denoted by $|M_{T_L}|$ hereafter) where $n_L = -\mathbf{e}_1$. Thus, $e_1^\top g_{k,i} > 0$. The new velocity and spatial position are given by

$$v_{k+1,i} = g_{k,i}, \quad x_{k+1,i} = L + \frac{x'_{k,i} - L}{e_1^\top v'_{k,i}} \, e_1^\top g_{k,i}. \tag{36}$$

- If $x'_{k,i} > R$, we sample $h_{k,i} \in \mathbb{R}^3$ from the half-Maxwellian flux $-v \cdot n_R \, M_{T_R}(v) \, \mathbb{1}_{v \cdot n_R < 0}$ (denoted by $-|M_{T_R}|$ hereafter) where $n_R = \mathbf{e}_1$. Thus, $e_1^\top h_{k,i} < 0$. The new velocity and spatial position are given by

$$v_{k+1,i} = h_{k,i}, \quad x_{k+1,i} = R + \frac{x'_{k,i} - R}{e_1^\top v'_{k,i}} \, e_1^\top h_{k,i}. \tag{37}$$

The position and velocity updates (36) and (37) do not include the possibility of multiple boundary crossings, but these can be easily added to the algorithm.

The algorithm in (36)-(37) is straightforward, but it results in a *random and discontinuous* change in particle velocity at the instant a particle interacts with the boundary. While this discontinuity is not problematic for forward DSMC simulations, it poses significant challenges for the derivation and implementation of adjoint DSMC methods.

We emphasize that this difficulty is not specific to the Boltzmann equation or to DSMC. More generally, for any evolution equation involving an advection operator that is solved using particle-based methods (or, equivalently, the method of characteristics), thermal BCs induce an instantaneous resampling of particle velocities at the boundary. This resampling produces an inherent discontinuity in the particle velocity at the time of boundary interaction. While such discontinuities are entirely benign for forward simulations, they present a fundamental challenge for adjoint-based sensitivity analysis and gradient computation, as classical differentiation across the boundary is no longer well defined.

To address this issue, we introduce a *stochastic modification* of the algorithm by replacing the deterministic time step Δt in (14) with a random variable τ. Specifically, we let τ follow a normal distribution $\mathcal{N}(\Delta t, \varepsilon^2)$, where Δt is the target time step and $\varepsilon \ll \Delta t/3$ is chosen so that the probability of $\tau < 0$ is negligible.

For fixed ε, this construction defines an ε-regularized DSMC scheme and an associated objective J_ε. Because the randomized time increment changes the probability of reaching the wall and the post-boundary particle position, the regularized and deterministic forward objectives need not agree exactly, even in expectation. As $\varepsilon \to 0$, however, the randomized update converges to the deterministic DSMC update. The numerical experiments in Section 6 examine the dependence of the objective and gradient on ε and show that the regularization effect is small over the range used in our calculations.

In the present work, this randomization of the boundary interaction serves as a numerical smoothing mechanism that enables the derivation of adjoint equations, which require differentiation of the particle velocity with respect to the particle position, despite the discontinuous dependence of velocity on position induced by the thermal BC. In other contexts, similar randomizations are introduced to model additional physical effects; here, however, the purpose is purely algorithmic.

The introduction of the random time step τ also has an important analytical consequence for the adjoint formulation. Because the boundary interaction is now described probabilistically, derivatives of expectations with respect to particle states can be computed using the score-function. In particular, sensitivities no longer require differentiating the discontinuous boundary map itself; instead, they involve differentiation of the log-density of τ, which is smooth. This replaces an ill-defined pathwise derivative at the boundary by a well-defined weak derivative in expectation. We now make this statement precise.

Under this modification, Line 9 of Algorithm 1, i.e., Equation (14), is replaced by

$$x'_{k,i} = x_{k,i} + \tau_{k,i}\,\mathcal{P}v'_{k,i}, \qquad \mathcal{P}v = e_1^\top v, \tag{38}$$

corresponding to the case of a 1D spatial domain and 3D velocity space. Since $\tau_{k,i}$ is a random variable, the three events $\{x'_{k,i} < L\}$, $\{x'_{k,i} \in \Omega\}$, and $\{x'_{k,i} > R\}$ occur with probabilities $p_l(x_{k,i}, v'_{k,i}; \Delta t, \varepsilon)$, $l = 1, 2, 3$, respectively. They sum to one: $\sum_{l=1}^{3} p_l(x_{k,i}, v'_{k,i}; \Delta t, \varepsilon) = 1$. Explicit formulas for $p_l(x, v; \Delta t, \varepsilon)$ are provided in Appendix A.

Within each global time interval $[t_k, t_{k+1}]$, collisions are first performed using the particle states synchronized at t_k. The particles are then advanced through the advection and boundary update, with the randomized time used only in this latter step; after the update, all particles are assigned to the common discrete time t_{k+1}.

Since Δt and ε are fixed hyperparameters, we henceforth write $p_l(x_{k,i}, v'_{k,i})$ for notational convenience. If $x'_{k,i} < L$ or $x'_{k,i} > R$, the updated velocity and position $(v_{k+1,i}, x_{k+1,i})$ are determined according to (36) and (37), respectively. Otherwise, the particle remains inside the domain and we set $x_{k+1,i} = x'_{k,i}$ and $v_{k+1,i} = v'_{k,i}$.

For any test function $\varphi(x, v)$, the conditional expectation of the post-update state satisfies

$$\begin{aligned} & \mathbb{E}_{\tau_{k,i}}\left[\varphi(x_{k+1,i}, v_{k+1,i}) \,\middle|\, (x_{k,i}, v'_{k,i})\right] \qquad (39)\\ = \;& p_1\big(x_{k,i}, v'_{k,i}\big)\, \mathbb{E}_{\tau_{k,i}}\mathbb{E}_{g_{k,i}}\left[\varphi\left(L + \frac{x'_{k,i} - L}{e_1^\top v'_{k,i}}\, e_1^\top g_{k,i},\; g_{k,i}\right) \,\middle|\, (x_{k,i}, v'_{k,i})\right] + \\ & p_2\big(x_{k,i}, v'_{k,i}\big)\, \mathbb{E}_{\tau_{k,i}}\left[\varphi(x'_{k,i}, v'_{k,i}) \,\middle|\, (x_{k,i}, v'_{k,i})\right] + \\ & p_3\big(x_{k,i}, v'_{k,i}\big)\, \mathbb{E}_{\tau_{k,i}}\mathbb{E}_{h_{k,i}}\left[\varphi\left(R + \frac{x'_{k,i} - R}{e_1^\top v'_{k,i}}\, e_1^\top h_{k,i},\; h_{k,i}\right) \,\middle|\, (x_{k,i}, v'_{k,i})\right], \end{aligned}$$

where $x'_{k,i}$ depends on $\tau_{k,i}$ through (38). Equation (39) highlights that, in a 1D spatial domain, each of the three possible post-update scenarios contributes two distinct sources of dependence on the pre-update state $(x_{k,i}, v'_{k,i})$:

(i) the probabilities $p_l(x_{k,i}, v'_{k,i})$, $l = 1, 2, 3$, and

(ii) the observable φ evaluated at $(x_{k+1,i}, v_{k+1,i})$.

The probabilistic decomposition in (39) is closely related to the probabilistic structure arising in DSMC methods that employ *virtual collisions* to efficiently and accurately sample collision events. In that setting, three mutually exclusive outcomes are considered, (1) no virtual collision, (2) a virtual collision that corresponds to a real collision, and (3) a virtual collision that does not result in a real collision, each occurring with a prescribed probability; see [25, Eqns. (11)-(13)]. A key contribution of our previous work [25] was the use of the score-function method [22] to account for the sensitivity of such probability terms with respect to optimization parameters. This approach enables accurate gradient computation in adjoint DSMC methods, even when the underlying dynamics involve discrete probabilistic branching, as in the present thermal boundary setting.

4.1. The Lagrangian

Similar to steps in Section 3, we first write down the Lagrangian to include the constraints. We denote the expectations over the step size τ_k in the kth time step by $\mathbb{E}_{\tau_{k,i}}$, and the expectations over the new velocities drawn from the thermal boundary condition by $\mathbb{E}_{g_{k,i},h_{k,i}}$. We define $\mathbb{E}^k = \mathbb{E}_{\{\tau_{k,i}\}}\mathbb{E}_{\{g_{k,i}\},\{h_{k,i}\}}$, the expectation over all random time steps and the wall emitted velocities, and $\mathbb{E}$ as

$$\mathbb{E} = \mathbb{E}^0\mathbb{E}^1\cdots\mathbb{E}^{M-1}.$$

Due to the introduction of stochastic time steps, we need to modify $\mathcal{J}_1$ and $\mathcal{J}_3$ in (22) and (24), respectively:

$$\mathcal{J}_1^{t1} = \frac{1}{N}\sum_{i=1}^{N} \mathbb{E}\left[r(x_{M,i}, v_{M,i})\right], \qquad (40)$$

$$\begin{aligned} \mathcal{J}_3^{t1} =& \frac{1}{N}\sum_{k=0}^{M-1}\sum_{i=1}^{N} \mathbb{E}^k\left[\beta_{k+1,i}\cdot\left(v_{k+1,i} - \mathcal{R}^v\left(x_{k,i}\,,\, v'_{k,i}\right)\right) \,\middle|\, (\mathcal{V}_k, \mathcal{X}_k)\right] + \qquad (41)\\ & \frac{1}{N}\sum_{k=0}^{M-1}\sum_{i=1}^{N} \mathbb{E}^k\left[\alpha_{k+1,i}\cdot\left(x_{k+1,i} - \mathcal{R}^x\left(x_{k,i}\,,\, v'_{k,i}\right)\right) \,\middle|\, (\mathcal{V}_k, \mathcal{X}_k)\right]. \end{aligned}$$

The operator $\mathcal{R}(x,v) = (\mathcal{R}^x(x,v), \mathcal{R}^v(x,v))$ enforces the thermal BC as follows: Define the three branch maps $\mathcal{R}_\ell(x,v;\tau,g,h) = (\mathcal{R}^x_\ell, \mathcal{R}^v_\ell)$ by

$$\mathcal{R}_1(x,v;\tau,g) = \begin{bmatrix} \left(1 - \frac{\mathcal{P}g}{\mathcal{P}v}\right) L + \frac{\mathcal{P}g}{\mathcal{P}v}\, x + \tau\, \mathcal{P}g \\ g \end{bmatrix}, \qquad \mathcal{R}_2(x,v;\tau) = \begin{bmatrix} x + \tau\, \mathcal{P}v \\ v \end{bmatrix},$$

$$\mathcal{R}_3(x,v;\tau,h) = \begin{bmatrix} \left(1 - \frac{\mathcal{P}h}{\mathcal{P}v}\right) R + \frac{\mathcal{P}h}{\mathcal{P}v}\, x + \tau\, \mathcal{P}h \\ h \end{bmatrix}.$$

The event $\ell \in \{1,2,3\}$ is selected according to the probabilities $p_\ell(x,v';\Delta t,\varepsilon)$ induced by $\tau \sim \mathcal{N}(\Delta t, \varepsilon^2)$, namely $\ell = 1$ if $x + \tau\mathcal{P}v' < L$, $\ell = 2$ if $L \le x + \tau\mathcal{P}v' \le R$, and $\ell = 3$ if $x + \tau\mathcal{P}v' > R$. Here, $\mathcal{P}$ is the projection onto the first component for the 1D spatial domain. Each term in $\mathcal{J}_3^{t1}$ should be interpreted following (39) for a particular function φ.

4.2. Adjoint equation derivation

With these preparations, we will derive the optimality conditions for the Lagrangian

$$\mathcal{J} = \mathcal{J}_1^{t1} + \mathcal{J}_2 + \mathcal{J}_3^{t1}\,,$$

combining terms in (40), (23) and (41).

4.2.1. Recovering forward DSMC

The collision and advection rules are derived from the derivatives of $\mathcal{J}$ with respect to $\beta_{k,i}$ and $\alpha_{k,i}$ for $k = 0,\dots,M-1$, and $i = 1,\dots,N$. Similarly, we recover the initial conditions for $x_{0,i}$ and $v_{0,i}$, $i = 1,\dots,N$.

4.2.2. Gradient for m

The gradient computation still follows Equations (32).

4.2.3. Final-time condition for the adjoint system

For each i, we take the derivative of $\mathcal{J}$ with respect to the final velocity particle $v_{M,i}$ and the final location $x_{M,i}$. Recall that

$$\mathcal{J}_1^{t1} = \frac{1}{N}\mathbb{E}\left[\sum_{i=1}^N r(x_{M,i}, v_{M,i})\right] \approx \frac{1}{N}\mathbb{E}\left[\sum_{i=1}^N r(x_{M,i}, v_{M,i})|(\mathcal{V}_M, \mathcal{X}_M)\right] = \frac{1}{N}\sum_{i=1}^N r(x_{M,i}, v_{M,i})\,.$$

We then have

$$\frac{\partial \mathcal{J}_1^{t1}}{\partial v_{M,i}} = \frac{1}{N}\partial_v r(x_{M,i}, v_{M,i})\,, \quad \frac{\partial \mathcal{J}_1^{t1}}{\partial x_{M,i}} = \frac{1}{N}\partial_x r(x_{M,i}, v_{M,i})\,.$$

For $\mathcal{J}_3^{t1}$ enforcing the binary collision and the advection rules, since the expectation $\mathbb{E}^{M-1}$ does not depend on particles in $\mathcal{V}_M$ and spatial positions in $\mathcal{X}_M$, we have

$$\frac{\partial \mathcal{J}_3^{t1}}{\partial v_{M,i}} = \frac{1}{N}\mathbb{E}^{M-1}[\beta_{M,i}|\,(\mathcal{V}_{M-1}, \mathcal{X}_{M-1})]\,, \quad \frac{\partial \mathcal{J}_3^{t1}}{\partial x_{M,i}} = \frac{1}{N}\mathbb{E}^{M-1}[\alpha_{M,i}|\,(\mathcal{V}_{M-1}, \mathcal{X}_{M-1})]\,.$$

The other terms in $\mathcal{J}$ do not depend on the particle positions $\mathcal{X}_M$ and velocities $\mathcal{V}_M$ at the final time, and so do not contribute to the derivatives. Summarizing all the terms and setting $\frac{\partial \mathcal{J}}{\partial v_{M,i}} = \frac{\partial \mathcal{J}}{\partial x_{M,i}} = 0$, we obtain the same final conditions (28)-(29).

4.2.4. Adjoint equations

Next, we derive the key equations for $\alpha_{k,i}$ and $\beta_{k,i}$ where $0 \le k \le M-1$. For $\mathcal{J}_1^{t1}$, we observe that, for any $k = 0, \dots, M-1$,

$$\begin{aligned}
\partial_{x_{k,i}} \mathcal{J}_1^{t1} &= \frac{1}{N} \partial_{x_{k,i}} \mathbb{E}^k \cdots \mathbb{E}^{M-1} \left[\sum_{j=1}^{N} r(x_{M,j}, v_{M,j}) \,\middle|\, (\mathcal{V}_k, \mathcal{X}_k) \right] \\
&= \frac{1}{N} \sum_{j=1}^{N} (\partial_{x_{k,i}} \mathbb{E}^k) \mathbb{E}^{k+1} \cdots \mathbb{E}^{M-1} \left[r(x_{M,j}, v_{M,j}) \,|\, (\mathcal{V}_k, \mathcal{X}_k) \right] \\
&= \frac{1}{N} \sum_{j=1}^{N} \mathbb{E}^k \cdots \mathbb{E}^{M-1} \left[\delta_{ji} \left(\partial_{x_{k,i}} \log p_l(x_{k,j}, v'_{k,j}) \right) r(x_{M,j}, v_{M,j}) \,\middle|\, (\mathcal{V}_k, \mathcal{X}_k) \right] \\
&= \frac{1}{N} \mathbb{E}^k \cdots \mathbb{E}^{M-1} \left[\left(\partial_{x_{k,i}} \log p_l(x_{k,i}, v'_{k,i}) \right) r(x_{M,i}, v_{M,i}) \,\middle|\, (\mathcal{V}_k, \mathcal{X}_k) \right]. \qquad (42)
\end{aligned}$$

Here, we used the identity $\partial_\theta \int f(x) p(x,\theta)\, dx = \int f(x) \left(\partial_\theta \log p(x,\theta)\right) p(x,\theta)\, dx$. In practice, we approximate the conditional expectation in (42) by a single-trajectory estimator, yielding

$$\partial_{x_{k,i}} \mathcal{J}_1^{t1} \approx \frac{1}{N} \left(\partial_{x_{k,i}} \log p_l(x_{k,i}, v'_{k,i}) \right) r_i, \qquad (43)$$

where $r_i := r(x_{M,i}, v_{M,i})$.

Similarly,

$$\begin{aligned}
\partial_{v_{k,i}} \mathcal{J}_1^{t1} &= \frac{1}{N} \partial_{v_{k,i}} \mathbb{E}^k \cdots \mathbb{E}^{M-1} \left[\sum_{j=1}^{N} r(x_{M,j}, v_{M,j}) \,\middle|\, (\mathcal{V}_k, \mathcal{X}_k) \right] \\
&= \frac{1}{N} \sum_{j=1}^{N} (\partial_{v_{k,i}} \mathbb{E}^k) \mathbb{E}^{k+1} \cdots \mathbb{E}^{M-1} \left[r(x_{M,j}, v_{M,j}) \,|\, (\mathcal{V}_k, \mathcal{X}_k) \right] \\
&= \frac{1}{N} \sum_{j=1}^{N} \mathbb{E}^k \cdots \mathbb{E}^{M-1} \left[(\delta_{ji_1} + \delta_{ji}) \left(\partial_{v_{k,i}} \log p_l(x_{k,j}, v'_{k,j}) \right) r(x_{M,j}, v_{M,j}) \,\middle|\, (\mathcal{V}_k, \mathcal{X}_k) \right] \\
&= \frac{1}{N} \mathbb{E}^k \cdots \mathbb{E}^{M-1} \Big[\left(\partial_{v_{k,i}} \log p_l(x_{k,i}, v'_{k,i}) \right) r_i + \left(\partial_{v_{k,i}} \log p_l(x_{k,i_1}, v'_{k,i_1}) \right) r_{i_1} \;\Big|\; (\mathcal{V}_k, \mathcal{X}_k) \Big].
\end{aligned}$$

In practice, we approximate the conditional expectation in the last term above by a single-trajectory estimator and apply the chain rule through the collision map, obtaining

$$\partial_{v_{k,i}} \mathcal{J}_1^{t1} \approx \frac{1}{N} \Big[\left(\partial_{v_{k,i}} v'_{k,i} \right)^\top \left(\partial_{v'_{k,i}} \log p_l(x_{k,i}, v'_{k,i}) \right) r_i + \left(\partial_{v_{k,i}} v'_{k,i_1} \right)^\top \left(\partial_{v'_{k,i_1}} \log p_l(x_{k,i_1}, v'_{k,i_1}) \right) r_{i_1} \Big]. \qquad (44)$$

Here, particles with indices i and i_1 form a collision pair at the kth time step. Explicit expressions for $\partial_v \log p_l(x,v)$ and $\partial_x \log p_l(x,v)$ are provided in Appendix A.

Next, we differentiate $\mathcal{J}_3^{t1}$ with respect to $x_{k,i}$ and $v_{k,i}$. Throughout, we view $\alpha_{k,i}$ and $\beta_{k,i}$ as column vectors, so Jacobians act on the adjoint variables through their transposes.

We obtain

$$\partial_{x_{k,i}}\mathcal{J}_3^{t1} = \frac{1}{N}\alpha_{k,i} - \frac{1}{N}\big(D_x\mathcal{R}^x_{k,i}\big)^\top\alpha_{k+1,i} - \frac{1}{N}\big(D_x\mathcal{R}^v_{k,i}\big)^\top\beta_{k+1,i}, \tag{45}$$

$$\begin{aligned}\partial_{v_{k,i}}\mathcal{J}_3^{t1} = {}& \frac{1}{N}\beta_{k,i} - \frac{1}{N}\Big(\partial_{v_{k,i}}v'_{k,i}\Big)^\top\big(D_v\mathcal{R}^v_{k,i}\big)^\top\beta_{k+1,i} - \frac{1}{N}\Big(\partial_{v_{k,i}}v'_{k,i_1}\Big)^\top\big(D_v\mathcal{R}^v_{k,i_1}\big)^\top\beta_{k+1,i_1}\\ & - \frac{1}{N}\Big(\partial_{v_{k,i}}v'_{k,i}\Big)^\top\big(D_v\mathcal{R}^x_{k,i}\big)^\top\alpha_{k+1,i} - \frac{1}{N}\Big(\partial_{v_{k,i}}v'_{k,i_1}\Big)^\top\big(D_v\mathcal{R}^x_{k,i_1}\big)^\top\alpha_{k+1,i_1}.\end{aligned} \tag{46}$$

Here we use the shorthand Jacobian notation

$$\begin{aligned} D_x\mathcal{R}^v_{k,i} &:= \frac{\partial\mathcal{R}^v}{\partial x}(x_{k,i}, v'_{k,i}), \qquad & D_x\mathcal{R}^x_{k,i} &:= \frac{\partial\mathcal{R}^x}{\partial x}(x_{k,i}, v'_{k,i}),\\ D_v\mathcal{R}^v_{k,i} &:= \frac{\partial\mathcal{R}^v}{\partial v}(x_{k,i}, v'_{k,i}), \qquad & D_v\mathcal{R}^v_{k,i_1} &:= \frac{\partial\mathcal{R}^v}{\partial v}(x_{k,i_1}, v'_{k,i_1}),\\ D_v\mathcal{R}^x_{k,i} &:= \frac{\partial\mathcal{R}^x}{\partial v}(x_{k,i}, v'_{k,i}), \qquad & D_v\mathcal{R}^x_{k,i_1} &:= \frac{\partial\mathcal{R}^x}{\partial v}(x_{k,i_1}, v'_{k,i_1}).\end{aligned} \tag{47}$$

These are components of the Jacobian of $\mathcal{R}(x,v) = (\mathcal{R}^x(x,v), \mathcal{R}^v(x,v))$. When a wall collision occurs, the sampled thermal velocity (g or h) is treated as *frozen* inside the derivative (i.e., we differentiate the map conditional on the sampled draw). Under this convention,

$$D_{(x,v)}\mathcal{R}(x,v) = \begin{cases} \begin{bmatrix} D_x\mathcal{R}^x(x,v) & D_v\mathcal{R}^x(x,v) \\ 0 & 0 \end{bmatrix}, & x < L,\ g \sim |M_{T_L}|,\\ \begin{bmatrix} I & \tau\,\mathcal{P} \\ 0 & I \end{bmatrix}, & L \le x \le R,\\ \begin{bmatrix} D_x\mathcal{R}^x(x,v) & D_v\mathcal{R}^x(x,v) \\ 0 & 0 \end{bmatrix}, & x > R,\ h \sim -|M_{T_R}|. \end{cases} \tag{48}$$

Moreover, in the left-wall case ($x + \tau\mathcal{P}v < L$) we have

$$D_x\mathcal{R}^x(x,v) = \frac{\mathcal{P}g}{\mathcal{P}v}, \qquad D_v\mathcal{R}^x(x,v) = (L-x)\,\frac{\mathcal{P}g}{(\mathcal{P}v)^2}\,\mathcal{P},$$

and in the right-wall case ($x + \tau\mathcal{P}v > R$) the same formulas hold with (L, g) replaced by (R, h). Setting $\partial_{x_{k,i}}\mathcal{J} = 0$ and $\partial_{v_{k,i}}\mathcal{J} = 0$, we obtain the adjoint equations

$$\alpha_{k,i} = \big(D_x\mathcal{R}^x_{k,i}\big)^\top\alpha_{k+1,i} + \big(D_x\mathcal{R}^v_{k,i}\big)^\top\beta_{k+1,i} - \partial_x \log p_l(x_{k,i}, v'_{k,i})\, r_i, \tag{49}$$

$$\begin{bmatrix}\beta_{k,i}\\ \beta_{k,i_1}\end{bmatrix} = B_{k,i}\begin{bmatrix} \big(D_v\mathcal{R}^x_{k,i}\big)^\top\alpha_{k+1,i} + \big(D_v\mathcal{R}^v_{k,i}\big)^\top\beta_{k+1,i} - \partial_v \log p_l(x_{k,i}, v'_{k,i})\, r_i \\ \big(D_v\mathcal{R}^x_{k,i_1}\big)^\top\alpha_{k+1,i_1} + \big(D_v\mathcal{R}^v_{k,i_1}\big)^\top\beta_{k+1,i_1} - \partial_v \log p_l(x_{k,i_1}, v'_{k,i_1})\, r_{i_1} \end{bmatrix}. \tag{50}$$

Finally, we have derived the adjoint system for the thermal BC, (49)-(50) starting with the final conditions (28)-(29). We introduced a key ingredient of the framework by employing a random time step around Δt. Randomization is needed to regularize discontinuities arising from wall collisions, enabling gradient evaluation via the score-function method.

Remark 1 (Practical implementation)**.** *In practice, the randomization of the time step needs to be applied only to particles whose spatial bins lie within a small neighborhood of the boundary. Particles well inside the domain may be advanced using the deterministic step Δt without affecting the adjoint formulation. This localized treatment significantly reduces unnecessary random sampling while preserving the differentiable structure required for adjoint sensitivity analysis. It is an easy adaptation of the adjoint DSMC algorithm presented in this section.*

4.3. Derivatives with respect to thermal boundary parameters

We now derive gradients of the objective function with respect to parameters appearing in the thermal boundary conditions. Let the thermal velocities at the left and right boundaries be generated through reparameterizations

$$g = S_L(\theta_L, \epsilon), \qquad h = S_R(\theta_R, \epsilon'),$$

where $\epsilon, \epsilon' \sim \mathcal{Y}$ are drawn from a parameter-independent reference distribution, and S_L and S_R are deterministic maps pushing forward $\mathcal{Y}$ to the half-Maxwellian flux distributions at the left and right walls, respectively. Typical choices of θ_L and θ_R include the wall temperatures and prescribed tangential wall velocities. Under this representation, the sensitivities of the sampled thermal velocities are

$$\partial_{\theta_L} g = \partial_{\theta_L} S_L(\theta_L, \epsilon), \qquad \partial_{\theta_R} h = \partial_{\theta_R} S_R(\theta_R, \epsilon'). \tag{51}$$

For example, if the parameter θ_L or θ_R is the vector-valued temperature $T = [T^1, T^2, T^3]^\top$, we use the following explicit reparameterization of the half-Maxwellian flux. Let $U \sim \mathcal{U}(0,1)$ and $Z_2, Z_3 \sim \mathcal{N}(0,1)$ be independent of T. At the left and right boundaries, respectively, we set

$$g(T_L) = \begin{bmatrix} \sqrt{-2T_L^1 \log U} \\ \sqrt{T_L^2} Z_2 \\ \sqrt{T_L^3} Z_3 \end{bmatrix}, \qquad h(T_R) = \begin{bmatrix} -\sqrt{-2T_R^1 \log U'} \\ \sqrt{T_R^2} Z_2' \\ \sqrt{T_R^3} Z_3' \end{bmatrix}.$$

Consequently,

$$\partial_{T_L} g = \frac{1}{2} \operatorname{diag}\left(\frac{g_1}{T_L^1}, \frac{g_2}{T_L^2}, \frac{g_3}{T_L^3} \right), \qquad \partial_{T_R} h = \frac{1}{2} \operatorname{diag}\left(\frac{h_1}{T_R^1}, \frac{h_2}{T_R^2}, \frac{h_3}{T_R^3} \right).$$

Taking derivatives of the Lagrangian $\mathcal{J}$ with respect to θ_L and θ_R yields

$$\partial_{\theta_L} \mathcal{J} = -\frac{1}{N} \sum_{k=0}^{M-1} \sum_{i=1}^{N} \mathbb{E}^k \left[\beta_{k+1,i}^\top \, \partial_{\theta_L} \mathcal{R}^v(x_{k,i}, v'_{k,i}) + \alpha_{k+1,i}^\top \, \partial_{\theta_L} \mathcal{R}^x(x_{k,i}, v'_{k,i}) \,\middle|\, (\mathcal{V}_k, \mathcal{X}_k) \right], \tag{52}$$

$$\partial_{\theta_R} \mathcal{J} = -\frac{1}{N} \sum_{k=0}^{M-1} \sum_{i=1}^{N} \mathbb{E}^k \left[\beta_{k+1,i}^\top \, \partial_{\theta_R} \mathcal{R}^v(x_{k,i}, v'_{k,i}) + \alpha_{k+1,i}^\top \, \partial_{\theta_R} \mathcal{R}^x(x_{k,i}, v'_{k,i}) \,\middle|\, (\mathcal{V}_k, \mathcal{X}_k) \right]. \tag{53}$$

After sampling the random variables at time step k, the conditional expectations collapse to single trajectory evaluations. Moreover, only particles undergoing thermal BC contribute

to the gradients. Thus,

$$\partial_{\theta_L}\mathcal{J} = -\frac{1}{N}\sum_{k=0}^{M-1}\sum_{\substack{i:\\ x_{k,i}+\tau\mathcal{P}v'_{k,i}<L}}\Big[\beta_{k+1,i}^{\top}\,\partial_{\theta_L}\mathcal{R}^{v}(x_{k,i},v'_{k,i}) + \alpha_{k+1,i}^{\top}\,\partial_{\theta_L}\mathcal{R}^{x}(x_{k,i},v'_{k,i})\Big], \tag{54}$$

$$\partial_{\theta_R}\mathcal{J} = -\frac{1}{N}\sum_{k=0}^{M-1}\sum_{\substack{i:\\ x_{k,i}+\tau\mathcal{P}v'_{k,i}>R}}\Big[\beta_{k+1,i}^{\top}\,\partial_{\theta_R}\mathcal{R}^{v}(x_{k,i},v'_{k,i}) + \alpha_{k+1,i}^{\top}\,\partial_{\theta_R}\mathcal{R}^{x}(x_{k,i},v'_{k,i})\Big]. \tag{55}$$

When a left-wall collision occurs ($x+\tau\,\mathcal{P}v<L$), the reflection map depends on θ_L only through the sampled thermal velocity g. Treating the sampled draw as frozen inside the derivative, we obtain

$$\partial_{\theta_L}\begin{bmatrix}\mathcal{R}^{x}\\ \mathcal{R}^{v}\end{bmatrix} = \partial_g\mathcal{R}\;\partial_{\theta_L}g = \begin{bmatrix}\mathcal{P}\left(\dfrac{x-L}{\mathcal{P}v}+\tau\right)\\ I\end{bmatrix}\partial_{\theta_L}g. \tag{56}$$

Similarly, when a right-wall collision occurs ($x+\tau\,\mathcal{P}v>R$),

$$\partial_{\theta_R}\begin{bmatrix}\mathcal{R}^{x}\\ \mathcal{R}^{v}\end{bmatrix} = \partial_h\mathcal{R}\;\partial_{\theta_R}h = \begin{bmatrix}\mathcal{P}\left(\dfrac{x-R}{\mathcal{P}v}+\tau\right)\\ I\end{bmatrix}\partial_{\theta_R}h. \tag{57}$$

Here, $\partial_{\theta_L}g$ and $\partial_{\theta_R}h$ are given by (51).

The reparameterization above also accommodates moving thermal walls. Let

$$\Pi_\tau = I - \mathcal{P}^*\mathcal{P}$$

denote the projection onto the tangential velocity space. The walls are fixed in the normal direction, so their prescribed velocities satisfy $\mathcal{P}U_L = \mathcal{P}U_R = 0$. The diffusely re-emitted velocities in the laboratory frame can be written as

$$g(U_L,T_L) = \Pi_\tau U_L + \widetilde{g}(T_L), \qquad h(U_R,T_R) = \Pi_\tau U_R + \widetilde{h}(T_R),$$

where $\widetilde{g}$ and $\widetilde{h}$ are the corresponding half-Maxwellian samples in the wall frames. It follows that

$$\partial_{U_L}g = \Pi_\tau, \qquad \partial_{U_R}h = \Pi_\tau.$$

Because the wall velocity is purely tangential, $\mathcal{P}\Pi_\tau = 0$. Therefore it does not directly affect the reflected particle position in the present one-dimensional spatial geometry:

$$\partial_{U_L}\mathcal{R}^{x} = \partial_{U_R}\mathcal{R}^{x} = 0, \qquad \partial_{U_L}\mathcal{R}^{v} = \partial_{U_R}\mathcal{R}^{v} = \Pi_\tau.$$

Substitution into (54)-(55) gives

$$\nabla_{U_L}J = -\frac{1}{N}\sum_{k=0}^{M-1}\sum_{x_{k,i}+\tau\mathcal{P}v'_{k,i}<L}\Pi_\tau\beta_{k+1,i}, \tag{58}$$

$$\nabla_{U_R}J = -\frac{1}{N}\sum_{k=0}^{M-1}\sum_{x_{k,i}+\tau\mathcal{P}v'_{k,i}>R}\Pi_\tau\beta_{k+1,i}. \tag{59}$$

There is no direct $\alpha_{k+1,i}$ contribution because the tangential wall velocity does not enter $\mathcal{R}^x$. In addition, no new score-function term is required since the current boundary-crossing probabilities depend on the incoming particle state and the randomized time step, but not on the tangential velocity subsequently assigned at the wall. Indirect effects on later collisions and boundary interactions are included through the usual backward propagation of α and β.

For the symmetric Couette parameterization, for which we will show an example in Section 6.4,

$$U_L = -U_w \mathbf{e}_2, \qquad U_R = U_w \mathbf{e}_2.$$

The chain rule therefore gives

$$\frac{dJ}{dU_w} = -\mathbf{e}_2^\top \nabla_{U_L} J + \mathbf{e}_2^\top \nabla_{U_R} J = \frac{1}{N} \sum_{k=0}^{M-1} \sum_{x_{k,i}+\tau\mathcal{P}v'_{k,i}<L} \beta^2_{k+1,i} - \frac{1}{N} \sum_{k=0}^{M-1} \sum_{x_{k,i}+\tau\mathcal{P}v'_{k,i}>R} \beta^2_{k+1,i}, \quad (60)$$

where $\beta^2_{k+1,i}$ denotes the second component of the velocity adjoint $\beta_{k+1,i}$.

4.4. Summary

In this section, we derived an adjoint DSMC formulation for the Boltzmann equation with thermal boundary conditions. The main difficulty stems from the discontinuous velocity resampling induced by wall interactions, which obstructs classical adjoint differentiation. We resolved this by introducing a randomized time step around Δt, providing a regularization that smooths boundary interactions in expectation. The resulting adjoint computes the gradient of the regularized objective J_ε. Its relationship with the original deterministic DSMC objective is examined numerically through an ε-stability study in Section 6.

5. Ensemble-Adjoint DSMC Method With Inflow Boundary Conditions

In this section, we derive an ensemble-adjoint DSMC method for the Boltzmann equation with inflow boundary conditions. We consider a one-dimensional spatial domain $\Omega = [L, R]$ and a three-dimensional velocity domain. Inflow boundary conditions are imposed at $x = L$ and $x = R$, and the incoming velocities are sampled from the corresponding boundary flux distributions, for example, from half-Maxwellian fluxes [21, Sec. 6].

The principal difficulty is that a perturbation of an inflow parameter changes not only the velocities of the newly injected particles, but also their later cell memberships, the local particle counts, and the collision schedules. A pathwise adjoint that differentiates one realized sequence of cell memberships and collision pairs treats these discrete choices as frozen and therefore does not, in general, approximate the derivative of the expected DSMC objective. Here, we instead differentiate the ensemble evolution. The resulting backward equation is the adjoint of the linearized Boltzmann collision operator, while the derivative of the inflow source is evaluated using a local score of the incoming flux distribution.

The ensemble collision formulation builds directly on the continuous adjoint framework introduced in our earlier work [8]. In that work, the nonlinear collision operator was linearized around a general nonequilibrium distribution, its adjoint was derived in a weighted L^2 space, and the continuous adjoint was identified with a Fréchet derivative of the objective. The

earlier derivation was presented for the spatially homogeneous Boltzmann equation. The present formulation applies the same linearized collision-adjoint structure locally in every spatial cell and couples it to free transport, absorbing outflow, and parameter-dependent inflow sources. In this sense, the new method extends the continuous, or optimize-then-discretize, side of [8], while using DSMC particles to perform the forward simulation and the Monte Carlo quadrature of the backward collision integrals.

For an inflow distribution $g(v,t;\theta)$ depending on boundary parameters θ, the incoming particle flux is

$$(-v\cdot\mathbf{n})g(v,t;\theta)\mathbb{1}_{\{v\cdot\mathbf{n}<0\}},$$

where $\mathbf{n}$ is the outward unit normal. Thus, over a boundary segment of area ΔS and a time interval Δt, the expected number of particles with velocities in $[v, v+dv]$ is

$$dN = \Delta S\,\Delta t\,(-v\cdot\mathbf{n})g(v,t;\theta)\mathbb{1}_{\{v\cdot\mathbf{n}<0\}}\,dv.$$

In the one-dimensional spatial setting, we take $\Delta S = 1$. At each time step, let N_L and N_R denote the numbers of particles injected at the left and right boundaries, respectively. In the formulation considered below, N_L and N_R are evaluated at the boundary parameters and then held fixed during differentiation. Consequently, we differentiate the normalized distributions of the incoming particle states, but not the discontinuous dependence of the integer-valued injection counts on the boundary parameters.

Let $\mathfrak{L}_k$ and $\mathfrak{R}_k$ denote the particles injected during the interval $[t_k, t_{k+1}]$ through the left and right boundaries. At the left boundary, an incoming velocity $g_{k,i}$ and an entry time $\xi_{k,i}\sim\mathcal{U}([0,\Delta t])$ are sampled independently, and the particle state at time t_{k+1} is

$$v_{k+1,i} = g_{k,i}, \qquad x_{k+1,i} = L + \xi_{k,i}\,g_{k,i}\cdot e_1, \qquad i\in\mathfrak{L}_k. \tag{61}$$

Similarly, at the right boundary,

$$v_{k+1,i} = h_{k,i}, \qquad x_{k+1,i} = R + \xi_{k,i}\,h_{k,i}\cdot e_1, \qquad i\in\mathfrak{R}_k, \tag{62}$$

where $h_{k,i}\cdot e_1 < 0$. Particles transported outside $[L,R]$ are removed from the active forward population and make no subsequent contribution to the collision dynamics or the terminal objective.

5.1. Forward ensemble and linearized collision operator

Let $f_k^j(v) := f(t_k, x\in\Omega_j, v)$ denote the particle distribution in spatial cell Ω_j at time t_k, and let

$$N_k^j = |\mathcal{V}_k^j|, \qquad \rho_k^j = \frac{N_k^j}{N_0|\Omega_j|}, \qquad \mu_k^j = \rho_k^j\int_{\mathbb{S}^2} q(\sigma)\,d\sigma.$$

The forward DSMC solver uses the actual full-population value of N_k^j to determine the local collision frequency. The expected number of collision pairs in cell j during one time step is

$$a_k^j = \frac{N_k^j\Delta t\,\mu_k^j}{2}.$$

An integer realization of a_k^j is obtained using the rounding rule of the forward DSMC algorithm, and the collision particles are selected uniformly without replacement from $\mathcal{V}_k^j$.

To derive the ensemble adjoint, we perturb the distribution according to $f_k \mapsto f_k + \delta f_k$. Equivalently, wherever $f_k > 0$, we may write the multiplicative perturbation $\delta f_k = f_k \psi_k$. Following the notation of [8], the linearized operator associated with the multiplicative perturbation is

$$L[f_k]\psi_k = f_k^{-1}\left[Q(f_k, f_k\psi_k) + Q(f_k\psi_k, f_k)\right]. \tag{63}$$

Since the Boltzmann collision operator is quadratic, the equivalent additive first variation is

$$\delta Q(f_k, f_k) = Q(\delta f_k, f_k) + Q(f_k, \delta f_k) =: \mathcal{L}_{f_k}\delta f_k. \tag{64}$$

The two notations are related by

$$\mathcal{L}_{f_k}\delta f_k = f_k\, L[f_k]\psi_k, \qquad \delta f_k = f_k\psi_k.$$

Both terms in (64) are required. The first describes the collision of a perturbed target distribution with the unperturbed forward distribution, while the second describes the change in the collision-partner distribution and in the local collision rate. In particular, the dependence of the ensemble collision dynamics on the local particle count N_k^j is contained in this linearization. This is the contribution that is absent when one differentiates a single DSMC trajectory while holding its cell memberships and collision schedule fixed.

5.2. The ensemble adjoint equation

Consider a terminal objective of the form

$$J = \frac{1}{\mathcal{N}} \sum_{i \in \mathcal{I}_M} r(x_{M,i}, v_{M,i}), \qquad \mathcal{N} = N_0 + M(N_L + N_R), \tag{65}$$

where $\mathcal{I}_M$ is the set of particles active at the terminal time $T = M\Delta t$. We introduce the scalar ensemble adjoint

$$\lambda_k(x, v) = \frac{\delta J}{\delta f_k}(x, v).$$

The sign convention differs from the one adopted in our earlier work [8]. This convention gives the gradient formula in (71)-(72) below. The terminal condition is

$$\lambda_M(x, v) = \frac{r(x, v)}{\mathcal{N}}, \qquad (x, v) \in \Omega \times \mathbb{R}^3, \tag{66}$$

and $\lambda_M = 0$ outside Ω.

We first pull the adjoint backward through free transport and absorbing outflow. Define

$$\widetilde{\lambda}_{k+1}(x, v) = \mathbb{1}_{\{x + \Delta t\, v \cdot e_1 \in \Omega\}} \lambda_{k+1}(x + \Delta t\, v \cdot e_1, v). \tag{67}$$

The indicator in (67) sets the future value to zero when the corresponding particle leaves the domain.

For a collision between velocities v and w, let (v', w') denote the post-collision velocities. The adjoint of the linearized collision operator in cell j is

$$(\mathcal{L}^*_{f_k^j}\psi)(v) = \int_{\mathbb{R}^3} f_k^j(w) \int_{\mathbb{S}^2} q(\sigma)\Big[\psi(v') + \psi(w') - \psi(v) - \psi(w)\Big]\, d\sigma\, dw. \tag{68}$$

This is the same four-term gain-loss structure as the operator $L^*[f]$ derived in [8]. The only change is that it is applied to the local distribution f_k^j in each spatial cell. In particular, when $\delta f_k = f_k \psi_k$, the duality relation from the earlier work becomes

$$\big(L[f_k]\psi_k, \lambda_k\big)_{L^2(f_k\,dv)} = \big(\psi_k, L^*[f_k]\lambda_k\big)_{L^2(f_k\,dv)},$$

which is the continuous identity approximated by the collision-partner Monte Carlo sum below. The discrete collision-transport splitting used by the DSMC implementation is then approximated by

$$\lambda_k(x,v) = \widetilde{\lambda}_{k+1}(x,v) + \Delta t\,(\mathcal{L}^*_{f_k^j}\widetilde{\lambda}_{k+1})(x,v), \qquad x \in \Omega_j. \tag{69}$$

Equation (69) differentiates the expected collision evolution rather than the particular collision pairs selected in one forward realization. Thus, no derivative of an individual pair-selection index or hard cell-membership indicator appears in the backward equation.

5.3. Local score for the inflow boundary source

We next derive the derivative with respect to the inflow parameters. Let $b_L(v;\theta_L)$ and $b_R(v;\theta_R)$ denote the normalized left and right incoming flux densities. For a sufficiently regular function F, the score identity gives

$$\partial_{\theta_s}\mathbb{E}_{b_s(\cdot;\theta_s)}[F(V)] = \mathbb{E}_{b_s(\cdot;\theta_s)}\left[F(V)\,\partial_{\theta_s}\log b_s(V;\theta_s)\right], \qquad s \in \{L,R\}. \tag{70}$$

A particle injected during $[t_k, t_{k+1}]$ is already part of the particle distribution at time t_{k+1}. Its adjoint value therefore contains its complete future effect, including all later transport, collisions, and its possible terminal contribution. Applying (70) locally to each boundary source gives

$$\nabla_{\theta_L} J = \sum_{k=0}^{M-1} N_L\,\mathbb{E}\left[\lambda_{k+1}\big(L + \xi V\cdot e_1, V\big)\nabla_{\theta_L}\log b_L(V;\theta_L)\right], \tag{71}$$

$$\nabla_{\theta_R} J = \sum_{k=0}^{M-1} N_R\,\mathbb{E}\left[\lambda_{k+1}\big(R + \xi V\cdot e_1, V\big)\nabla_{\theta_R}\log b_R(V;\theta_R)\right], \tag{72}$$

where $\xi \sim \mathcal{U}([0,\Delta t])$ is independent of V. There is no additional score associated with ξ, because its distribution is parameter-independent. The sign in (71)-(72) is positive under the adjoint definition (66).

For the anisotropic zero-mean Maxwellian used in the numerical experiments, let $T_s = (T_{s,1}, T_{s,2}, T_{s,3})$. The normalized incoming flux density at the left boundary is

$$b_L(v;T_L) = \mathbb{1}_{\{v_1>0\}}\frac{v_1}{T_{L,1}}\exp\left(-\frac{v_1^2}{2T_{L,1}}\right)\prod_{\ell=2}^{3}\frac{1}{\sqrt{2\pi T_{L,\ell}}}\exp\left(-\frac{v_\ell^2}{2T_{L,\ell}}\right). \tag{73}$$

At the right boundary, $v_1 > 0$ is replaced by $v_1 < 0$ and v_1 by $|v_1|$. The componentwise temperature scores are

$$\partial_{T_{s,1}}\log b_s(v;T_s) = -\frac{1}{T_{s,1}} + \frac{v_1^2}{2T_{s,1}^2}, \tag{74}$$

$$\partial_{T_{s,\ell}}\log b_s(v;T_s) = -\frac{1}{2T_{s,\ell}} + \frac{v_\ell^2}{2T_{s,\ell}^2}, \qquad \ell = 2,3, \tag{75}$$

for $s \in \{L, R\}$. Since the normal score depends on v_1^2, the same formula applies at both boundaries; the boundary orientation is represented by the support of the corresponding half-range distribution.

If the physical injection intensity is also differentiated, then its derivative must be added separately. For example, for a zero-mean Maxwellian inflow with intensity $N_s(T_{s,1}) \propto \sqrt{T_{s,1}}$, the smooth intensity contribution adds $\partial_{T_{s,1}} \log N_s(T_{s,1}) = \frac{1}{2T_{s,1}}$ to (74). A parameter-dependent normalization $\mathcal{N}$ would introduce the corresponding quotient-rule term. These are not included in the formulation considered in (71)-(72).

5.4. Monte Carlo approximation of the backward equation

For a moderate particle population, the adjoint field may be represented on the complete sequence of forward particle populations, but sometimes, storing every particle at every time level is impractical. We therefore introduce a memory-bounded adjoint formulation without modifying the physical forward simulation.

At every time level and in every cell Ω_j, we retain a uniform sample $\widehat{\mathcal{V}}_k^j \subset \mathcal{V}_k^j$ containing at most N_{res} particles. The exact full-population cell count N_k^j is stored separately and is used in the collision coefficient. We also retain uniform samples $\widehat{\mathfrak{L}}_k \subset \mathfrak{L}_k$ and $\widehat{\mathfrak{R}}_k \subset \mathfrak{R}_k$ of the injected particles. If $m_{L,k} = |\widehat{\mathfrak{L}}_k|$, the corresponding weight is $N_L/m_{L,k}$, with an analogous definition on the right.

The adjoint is represented by scalar values on the retained states. A local interpolant $\mathcal{I}_k[\lambda_k](x, v)$ supplies the adjoint at other non-retained states, including the post-collision states and the injected source states. In the numerical implementation, the interpolant is a weighted local affine fit in (x, v_1, v_2, v_3) based on neighboring retained particles.

For a retained state $(x_{k,i}, v_{k,i}) \in \Omega_j$, we sample N_{col} collision-partner states $(x_{k,i_s}, w_{k,i}^{(s)})$ from the same cell and scattering directions $\sigma_{k,i}^{(s)}$ from the normalized angular kernel. Let $(v_{k,i}^{\prime(s)}, w_{k,i}^{\prime(s)})$ denote the corresponding post-collision velocities, and let $Q_0 = \int_{\mathbb{S}^2} q(\sigma)\, d\sigma$. The collision-adjoint correction is approximated by

$$\widehat{C}_{k,i} = \Delta t\, \rho_k^j Q_0\, \frac{1}{N_{\text{col}}} \sum_{s=1}^{N_{\text{col}}} \Big[\widetilde{\lambda}_{k+1}(x_{k,i}, v_{k,i}^{\prime(s)}) + \widetilde{\lambda}_{k+1}(x_{k,i_s}, w_{k,i}^{\prime(s)}) - \widetilde{\lambda}_{k+1}(x_{k,i}, v_{k,i}) - \widetilde{\lambda}_{k+1}(x_{k,i_s}, w_{k,i}^{(s)}) \Big]. \tag{76}$$

The adjoint update for this retained particle is therefore

$$\widehat{\lambda}_{k,i} = \widetilde{\lambda}_{k+1}(x_{k,i}, v_{k,i}) + \widehat{C}_{k,i}. \tag{77}$$

Although the velocity distribution inside a cell is represented by the retained states, the coefficient ρ_k^j in (76) is always computed using the exact full-population count N_k^j. Thus, using a subset of the states does not artificially reduce the local collision frequency.

The sampled left-boundary gradient is

$$\widehat{\nabla_{\theta_L} J} = \sum_{k=0}^{M-1} \frac{N_L}{m_{L,k}} \sum_{i \in \widehat{\mathfrak{L}}_k} \mathcal{I}_{k+1}[\widehat{\lambda}_{k+1}](x_{k+1,i}, v_{k+1,i}) \nabla_{\theta_L} \log b_L(v_{k+1,i}; \theta_L), \tag{78}$$

and the right-boundary gradient is obtained analogously. The expansion weights make these source sums unbiased conditional on the reconstructed adjoint field.

The complete procedure is summarized below.

(i) Run the full-population forward DSMC simulation. At every time level, store a subset of the particles, the exact cell counts, and weighted samples of the two inflow sources.

(ii) Initialize the terminal adjoint using (66).

(iii) For $k = M-1, \dots, 0$, construct the interpolant of the adjoint at t_{k+1}, accumulate the two local boundary-score contributions, pull the adjoint backward through transport and absorbing outflow (67), and apply the Monte Carlo collision correction (76).

(iv) Sum the boundary-source contributions over all time steps to obtain the left and right parameter gradients; see (78).

For a scalar objective, only one scalar backward field is required. After one backward adjoint solve, the adjoint is evaluated once at each sampled incoming state. The gradient with respect to each boundary parameter is then obtained by multiplying these adjoint values by the corresponding source-score components and summing over the incoming samples. Consequently, the dominant forward- and backward-DSMC costs are independent of the number of inflow parameters.

6. Numerical Examples

All numerical examples in this section are conducted on a 1D spatial domain $\Omega = [0,1] \subset \mathbb{R}$ and a 3D velocity domain $\mathbb{R}^3$. The Knudsen number in all examples is chosen to be 1. We consider four numerical examples and verify the adjoint gradients by comparison with centered finite-difference approximations. The examples include two-sided thermal boundaries, mixed thermal-specular boundaries, two-sided inflow, and a high-Mach-number Couette flow driven by moving thermal walls.

6.1. Heat conduction: two-sided thermal BC

Our first example concerns heat conduction. We enforce thermal BC at the left boundary $x = 0$ and the right boundary point $x = 1$, both with half-Maxwellian flux distributions. The temperatures for the two half-Maxwellian fluxes are respectively

$$T_L = [T_L^1, T_L^2, T_L^3] = [0.6, 0.6, 0.6]\,, \qquad T_R = [T_R^1, T_R^2, T_R^3] = [0.9, 0.9, 0.9]\,. \tag{79}$$

The temperature difference induces a non-equilibrium heat flux across the domain. This setup provides a canonical test of thermal BC in kinetic simulations and allows us to assess whether the adjoint method correctly captures the sensitivity of energy transport with respect to boundary temperature parameters.

The initial distribution for the Boltzmann equation is set as

$$f_0(x,v) = \left(\frac{1}{\sqrt{2\pi}\sigma}\right)^3 \exp\left(-\frac{|v|^2}{2\sigma^2}\right)\,, \quad \sigma = 0.7\,.$$

Let N denote the total number of particles used in the forward DSMC. We draw i.i.d. samples $x_{0,i} \sim \mathcal{U}([0,1])$ and $v_{0,i} \sim \mathcal{N}(0,\sigma^2)$, $1 \le i \le N$, to approximate the initial distribution f_0.

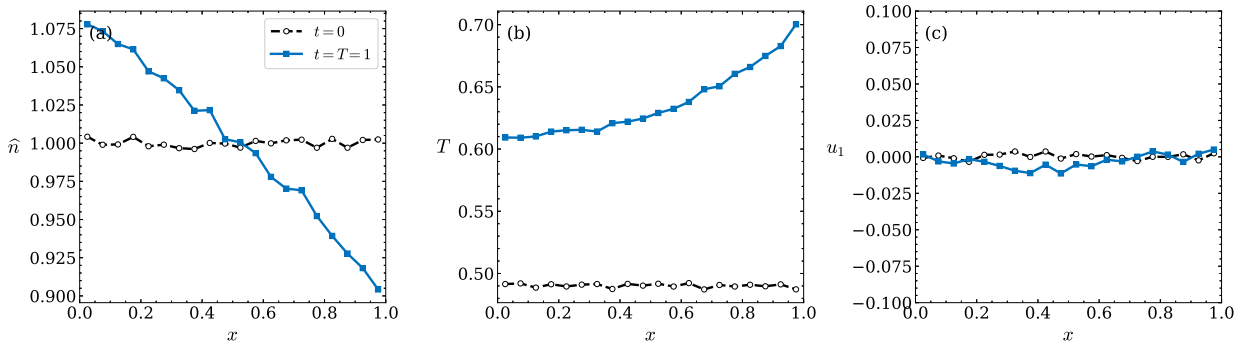


Figure 1: Two-sided thermal boundary conditions: profiles of (a) normalized number density $\widehat{n}$, (b) scalar temperature T, and (c) streamwise bulk velocity u_1 at $t = 0$ and $t = T = 1$. The simulation uses $N_0 = 2\times10^6$ and $\Delta x = 0.05$.

The total forward simulation time is $T = 1$ with $\Delta t = 0.1$. We discretize the spatial domain $[0, 1]$ into equal-size cells with $\Delta x \in \{0.05, 0.1, 0.2\}$. Here, we consider T_L and T_R as variables for an optimization problem with the objective function

$$J_1(T_L, T_R) = \int_0^1 \int_{\mathbb{R}^3} |v|^2 e^{-(x-0.2)^2} f(x, v, T) dv dx \,,$$

where $f(x, v, T)$ is the Boltzmann equation solution at the final simulation time $T = 1$.

The objective J_1 measures the localized kinetic energy near $x = 0.2$, with the Gaussian weight emphasizing sensitivity to energy transport from the left boundary. Thus, the gradient $\nabla_{T_L,T_R} J_1$ quantifies how changes in boundary temperatures influence the spatial redistribution of energy inside the domain.

To illustrate the macroscopic state associated with the gradient test, Figure 1 shows the normalized number density $\widehat{n} = N_j/(N_0\Delta x)$, the scalar temperature $T = \langle|v - u|^2\rangle/3$, and the streamwise bulk velocity u_1 at the initial and final times. The profiles are obtained from one forward realization with $N_0 = 2 \times 10^6$ particles and $\Delta x = 0.05$. Initially, the density is uniform, the temperature is approximately $0.49 = 0.7^2$, and the bulk velocity is zero up to sampling error. At $T = 1$, the density decreases from approximately 1.08 near the left wall to 0.90 near the right wall, while the temperature increases from approximately 0.61 to 0.70 across the domain in response to the wall temperatures $T_L = 0.6$ and $T_R = 0.9$. The streamwise velocity remains small throughout the domain, with $|u_1| < 9 \times 10^{-3}$, indicating that the dominant nonequilibrium effect is thermal transport.

Following the algorithm derived in Section 4, we first modify the forward DSMC algorithm by replacing the deterministic time step size Δt with a random variable $\tau \sim \mathcal{N}(\Delta t, \varepsilon^2)$, where we set $\varepsilon = \Delta t/10 = 0.01$. This selective stochastic regularization smooths otherwise discontinuous boundary-interaction events while introducing only a small perturbation of the deterministic forward scheme for the chosen value of ε. To improve sampling efficiency, the random time step is applied only to particles that may interact with the boundary during the current update. Specifically, at each time level t_k, we examine the particle's current position $x_{k,i}$ and post-collision velocity $v'_{k,i}$. If

$$\text{dist}(x_{k,i}, \partial\Omega) < (\Delta t + 3\varepsilon)|\mathcal{P}v'_{k,i}| \,,$$

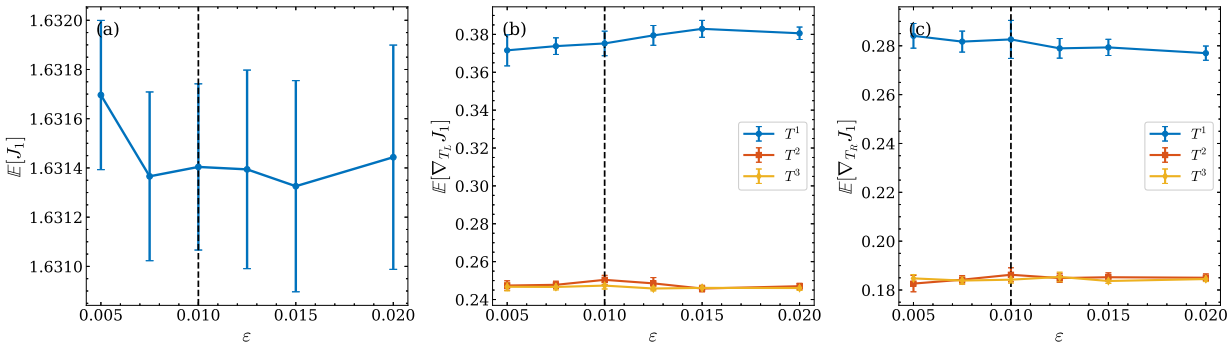


Figure 2: Dependence of (a) the mean objective J_1, (b) the mean adjoint gradient with respect to the left-wall temperature T_L, and (c) the mean adjoint gradient with respect to the right-wall temperature T_R on the regularization width ε. Error bars represent twice the standard error of the mean over 48 independent runs. The black dashed line marks $\varepsilon = \Delta t/10 = 0.01$, used in the main numerical experiments. The study uses $N = 10^6$ and $\Delta x = 0.1$.

then the particle is considered sufficiently close to the boundary that a boundary-crossing event could occur under a randomized update. In this case, the deterministic time step Δt is replaced by a random variable $\tau \sim \mathcal{N}(\Delta t, \varepsilon^2)$. For all other particles, whose trajectories remain well separated from the boundary over the current time increment, the deterministic time step Δt is retained. This selective stochastic regularization smooths otherwise discontinuous boundary interaction events, thereby enabling differentiation through boundary reflections while converging to the deterministic forward scheme as $\varepsilon \to 0$.

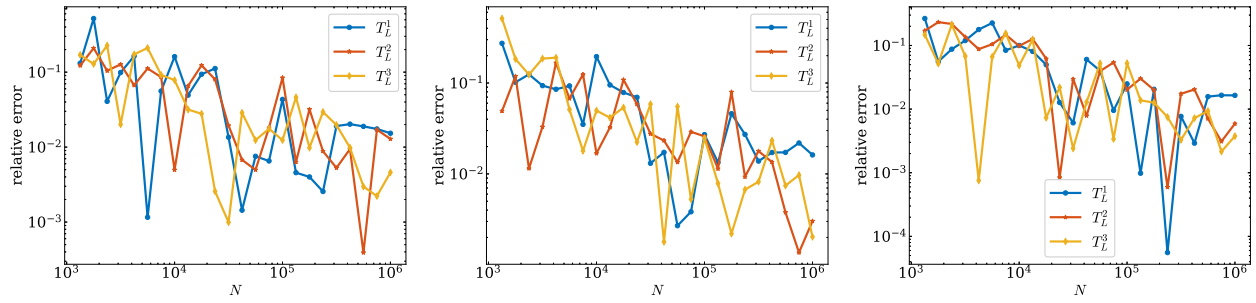
To assess the sensitivity of the regularized adjoint gradient to the regularization width, we repeat Test 1 with $N = 10^6$, $\Delta x = 0.1$, and $\varepsilon \in [0.005, 0.02]$, using 48 independent runs for each value. Figure 2 shows the resulting mean objective and adjoint gradients with respect to T_L and T_R, with error bars representing twice the standard error of the mean. The objective varies by less than 0.07% over the tested interval, while the gradient components exhibit no systematic dependence on ε within their Monte Carlo uncertainty. These results indicate that the regularized adjoint gradient is stable over the range of ε relevant to the numerical experiments, including the chosen value $\varepsilon = \Delta t/10 = 0.01$.

Next, using this modified forward DSMC algorithm, we implement the adjoint DSMC approach to compute the gradient with respect to the boundary temperature parameters T_L and T_R, denoted by $\nabla^{\mathrm{AJ}}_{T_L} J_1$ and $\nabla^{\mathrm{AJ}}_{T_R} J_1$, following the derived gradient formulae (54)-(55). To apply these equations, we compute the adjoint variable $\{\alpha_{k,i}\}$ and $\{\beta_{k,i}\}$ following the adjoint DSMC rule given in (49) and (50). The goal of the numerical experiment is therefore twofold: (i) to verify that the adjoint gradient agrees with a finite-difference benchmark, and (ii) to confirm that its variance exhibits the expected Monte Carlo scaling with respect to the number of particles N.

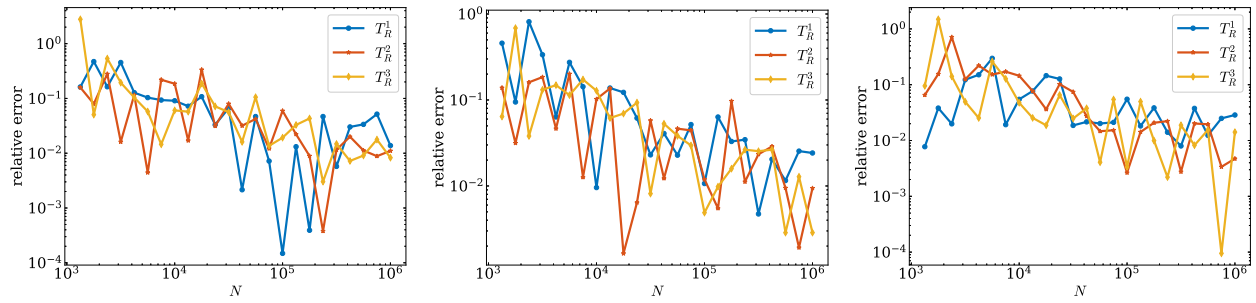
To verify the accuracy of the computed adjoint gradients, we compare them to gradients approximated using finite difference perturbations. For instance, to approximate $\partial_{T_L^1} J_1$, we employ a central difference scheme given by:

$$\nabla^{\mathrm{FD}}_{T_L^1} J_1 := \frac{J_1(T_L^1 + \delta) - J_1(T_L^1 - \delta)}{2\delta} \approx \partial_{T_L^1} J_1 \,,$$

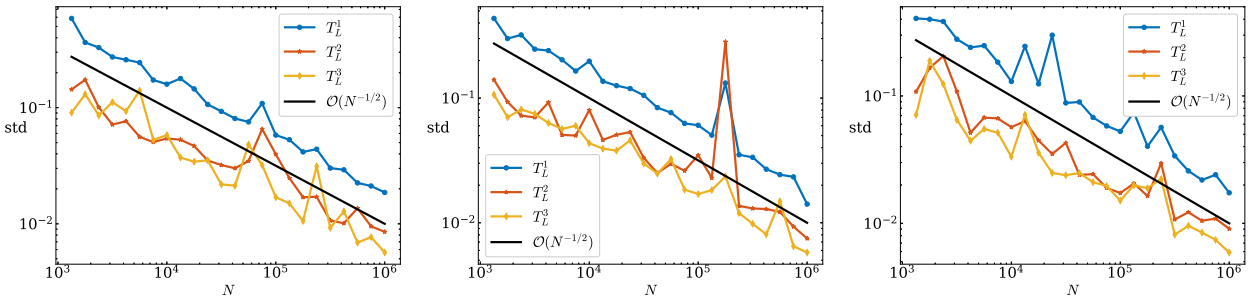
where $\delta = 0.025$ is fixed for all components of T_L and T_R. The finite-difference gradients



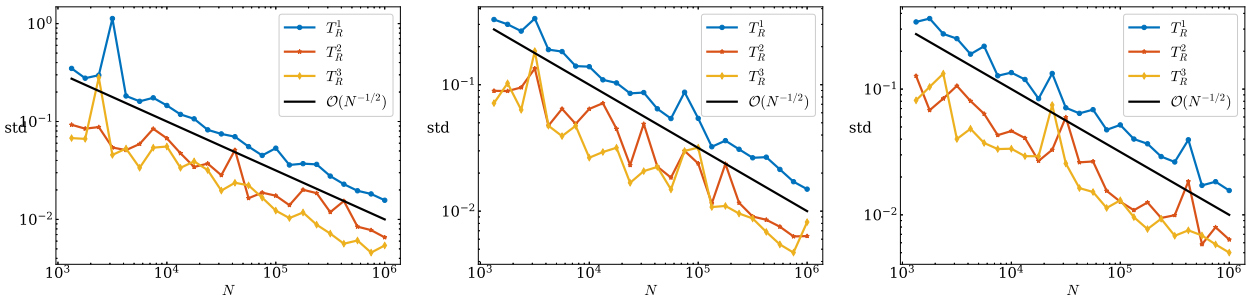
(a) $|\nabla^{\mathrm{AJ}}_{T_L} J_1 - \nabla^{\mathrm{FD}}_{T_L} J_1| / |\nabla^{\mathrm{FD}}_{T_L} J_1|$ for $\Delta x \in \{0.05, 0.1, 0.2\}$.



(b) $|\nabla^{\mathrm{AJ}}_{T_R} J_1 - \nabla^{\mathrm{FD}}_{T_R} J_1| / |\nabla^{\mathrm{FD}}_{T_R} J_1|$ for $\Delta x \in \{0.05, 0.1, 0.2\}$.



(c) standard deviation in $\nabla^{\mathrm{AJ}}_{T_L} J_1$ for $\Delta x \in \{0.05, 0.1, 0.2\}$



(d) standard deviation in $\nabla^{\mathrm{AJ}}_{T_R} J_1$ for $\Delta x \in \{0.05, 0.1, 0.2\}$

Figure 3: Thermal-thermal BCs (Section 6.1): (a) and (b) show the relative error between the adjoint gradient and the finite-difference gradient for T_L and T_R, respectively, as the number of particles N increases; (c) and (d) show the standard deviation of the adjoint gradient for T_L and T_R, respectively. The standard deviation decreases with N and is broadly consistent with the Monte Carlo $N^{-1/2}$ reference trend. The three columns correspond to different spatial bin sizes: from left to right, $\Delta x = 0.05$, 0.1, and 0.2, respectively.

are computed using the original DSMC scheme with deterministic time step Δt, whereas the adjoint gradient corresponds to the ε-regularized scheme. Thus, the comparison is between an adjoint approximation of ∇J_ε and a finite-difference approximation of ∇J_0. Agreement between the two estimators indicates that the regularization bias is small for the chosen value of ε, while the separate ε-stability experiment examines this dependence directly.

We range the number of particles N from 10^3 to 10^6 to examine the accuracy of the adjoint gradient. To further reduce random error, we conduct 96 independent runs for both the adjoint gradient and the finite-difference gradient and compare the mean value of these experimental outcomes. We also use these 96 runs to approximate the standard deviation. In the heat conduction example, we analyze the performance of the adjoint gradient computation in comparison to the finite-difference gradient approximation as the number of particles N increases. Figures 3a-3b illustrate the relative error between the adjoint gradient and the finite-difference gradient for the boundary temperature parameters T_L and T_R, respectively. As N increases, the error decreases, demonstrating consistency between the adjoint and finite-difference methods. Additionally, Figures 3c-3d show the standard deviation (std) of the adjoint gradient for T_L and T_R, respectively. This follows the expected Monte Carlo convergence rate of $\mathcal{O}(1/\sqrt{N})$ (plotted in black solid lines for reference).

The observed decay of both the bias (relative error) and variance confirms that the adjoint DSMC method produces statistically consistent gradient estimates, even in the presence of thermal boundary reflections. In particular, the $\mathcal{O}(1/\sqrt{N})$ variance scaling demonstrates that the stochastic boundary regularization does not degrade Monte Carlo efficiency. These results validate the robustness and practical feasibility of the proposed adjoint framework for sensitivity analysis in spatially inhomogeneous Boltzmann simulations with thermal BCs.

6.2. Mixed reflecting BC: thermal and specular reflections

In our second test, we consider a mixed BC: at the left boundary, $x = 0$, thermal BC is enforced with a non-isotropic left half-Maxwellian flux distribution with the temperature $T_L = [0.6, 0.5, 0.8]$ and at the right boundary $x = 1$, the specular reflection is enforced (see Section 3.2). This mixed configuration creates an asymmetric setting in which one boundary injects thermal fluctuations while the other preserves kinetic energy through deterministic reflection. As a result, the dynamics combine stochastic boundary resampling and deterministic mirror interactions.

We use the same objective function as in Section 6.1 but with the final time $T = 0.5$, which is denoted by J_2. The discretization parameters are $\Delta t = 0.05$, and $\Delta x = 0.1$. The initial condition is a uniform distribution over the spatial domain $\Omega = [0, 1]$ and a Maxwellian distribution in velocity with temperature $T_0^2 \cdot [1, 1, 1]$ where $T_0 = 1$. Similar to the example in Section 6.1, a random time step is applied only to particles that may interact with the left boundary (associated with the thermal BC) during the current update.

Figure 4 presents the corresponding macroscopic profiles for the mixed thermal-specular configuration, again using $N_0 = 2 \times 10^6$ and $\Delta x = 0.05$. The initial density and temperature are approximately uniform, with $\widehat{n} \simeq 1$ and $T \simeq 1$, and the initial bulk velocity is statistically indistinguishable from zero. By $T = 0.5$, particles accumulate near the thermal left wall, where the normalized density reaches approximately 1.14, while the density over most of the remaining domain is slightly below one. The temperature is lowest near the thermal wall,

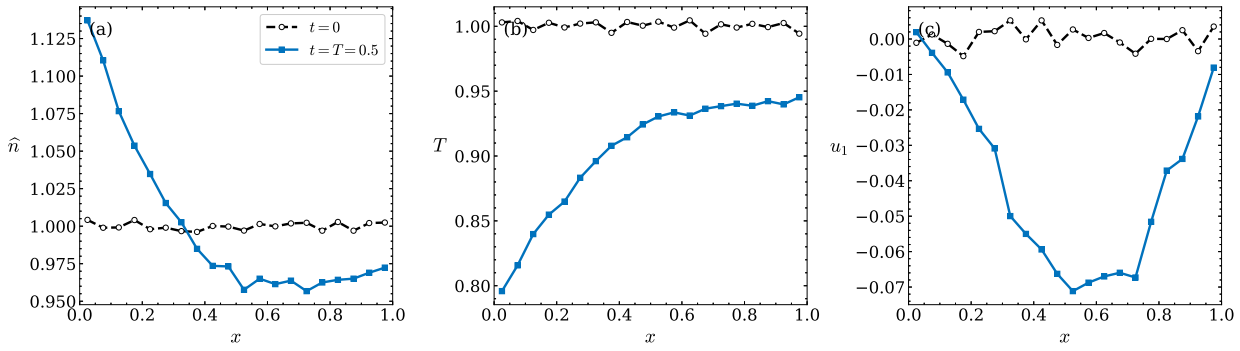


Figure 4: Mixed thermal and specular boundary conditions: profiles of (a) normalized number density $\widehat{n}$, (b) scalar temperature T, and (c) streamwise bulk velocity u_1 at $t = 0$ and $t = T = 0.5$. The simulation uses $N_0 = 2 \times 10^6$ and $\Delta x = 0.05$.

where it is approximately 0.80, and increases toward approximately 0.94 near the specular boundary. The resulting asymmetric transient produces a negative streamwise bulk velocity in the interior, with a minimum of approximately -0.072, whereas the initial velocity profile fluctuates only weakly around zero.

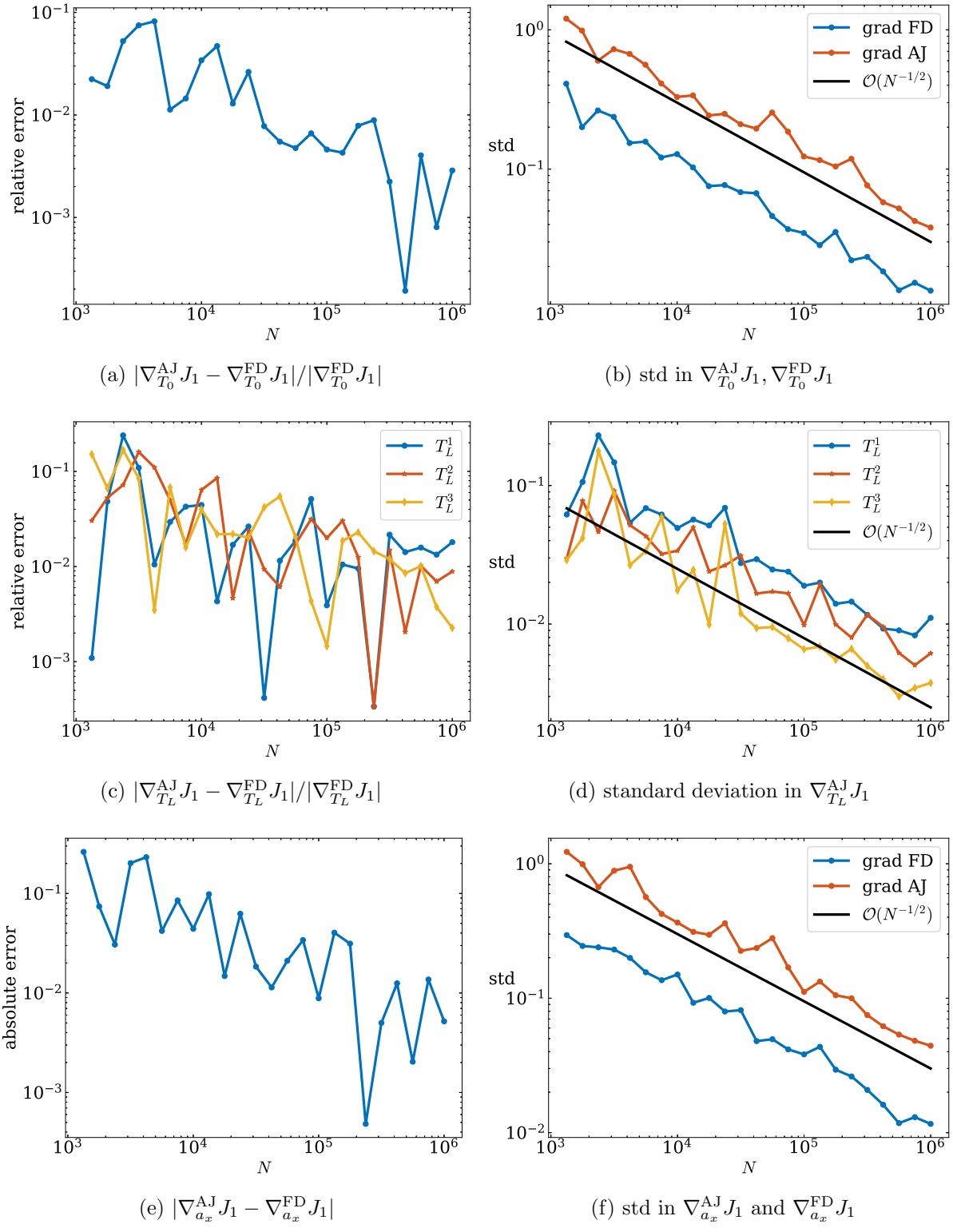
In this example, the objective depends both on boundary-driven energy injection (through T_L) and on the initial thermal state (through T_0). Consequently, the gradients $\nabla_{T_L} J$ and $\nabla_{T_0} J$ measure distinct physical sensitivities: the former captures the influence of boundary heating, while the latter quantifies how perturbations of the initial kinetic energy propagate over time under mixed reflection mechanisms.

We use the adjoint DSMC method to compute the gradients with respect to the thermal BC parameter T_L and the initial distribution's parameter T_0. The results are then compared with the finite-difference approximation with the perturbation $\delta = 0.05$. The number of particles in the forward and adjoint DSMC ranges from $N = 10^3$ to $N = 10^6$. We use 42 i.i.d. runs to approximate the standard deviation of all gradients, and compare the difference between the mean values. Because specular reflection is deterministic and smooth with respect to particle states, no stochastic regularization is required at the right boundary. Therefore, this experiment isolates the effect of the thermal boundary regularization at $x = 0$ and allows us to verify that the adjoint treatment remains accurate even when different reflection mechanisms coexist.

We plot both the error decay and standard deviation change in the finite-difference gradients $\nabla_{T_0}^{\mathrm{FD}}$, $\nabla_{T_L}^{\mathrm{FD}}$ and the adjoint DSMC gradients $\nabla_{T_0}^{\mathrm{AJ}}$, $\nabla_{T_L}^{\mathrm{AJ}}$ in Figure 5. The observed convergence confirms that the adjoint DSMC method remains statistically consistent in the presence of mixed boundary conditions. In particular, the preservation of the $\mathcal{O}(1/\sqrt{N})$ variance scaling demonstrates that combining stochastic (thermal) and deterministic (specular) reflections does not introduce additional variance beyond standard Monte Carlo sampling error. These results further support the robustness of the adjoint framework for sensitivity analysis in heterogeneous boundary configurations.

To further examine sensitivity with respect to the initial spatial distribution, we introduce a scalar shape parameter $a_x > 0$ and define

$$\rho_0(x; a_x) = a_x x^{a_x - 1}, \qquad x \in [0, 1].$$



(a) $|\nabla^{\mathrm{AJ}}_{T_0} J_1 - \nabla^{\mathrm{FD}}_{T_0} J_1| / |\nabla^{\mathrm{FD}}_{T_0} J_1|$

(b) std in $\nabla^{\mathrm{AJ}}_{T_0} J_1, \nabla^{\mathrm{FD}}_{T_0} J_1$

(c) $|\nabla^{\mathrm{AJ}}_{T_L} J_1 - \nabla^{\mathrm{FD}}_{T_L} J_1| / |\nabla^{\mathrm{FD}}_{T_L} J_1|$

(d) standard deviation in $\nabla^{\mathrm{AJ}}_{T_L} J_1$

(e) $|\nabla^{\mathrm{AJ}}_{a_x} J_1 - \nabla^{\mathrm{FD}}_{a_x} J_1|$

(f) std in $\nabla^{\mathrm{AJ}}_{a_x} J_1$ and $\nabla^{\mathrm{FD}}_{a_x} J_1$

Figure 5: Thermal and specular reflections BCs (Section 6.2): (a), (c) and (e) show the error between the adjoint gradient and the finite-difference gradient for T_0, T_L and a_x, respectively, as the number of particles N increases; (b), (d) and (f) show the standard deviation of the gradients with respect to these parameters, respectively. The standard deviation decays with a rate of $\mathcal{O}(\frac{1}{\sqrt{N}})$.

The value $a_x = 1$ recovers the uniform spatial distribution used in the original setup. Samples from this family are generated through the inverse-transform representation

$$X_{0,i} = U_i^{1/a_x}, \qquad U_i \sim \mathcal{U}(0,1),$$

for which

$$\frac{\partial X_{0,i}}{\partial a_x} = -\frac{X_{0,i} \log U_i}{a_x^2}.$$

After propagating the position adjoint variables backward to the initial time, we combine them with these derivatives to obtain $\nabla_{a_x}^{\mathrm{AJ}} J_2$. We compare this result with the centered finite-difference approximation

$$\nabla_{a_x}^{\mathrm{FD}} J_2 = \frac{J_2(a_x + \delta) - J_2(a_x - \delta)}{2\delta}, \qquad \delta = 0.05.$$

The same uniform samples $\{U_i\}$ and random seeds are used for both perturbations to provide common random numbers.

Figure 5e shows the absolute discrepancy

$$\left|\nabla_{a_x}^{\mathrm{AJ}} J_2 - \nabla_{a_x}^{\mathrm{FD}} J_2\right|$$

as the number of particles increases. We report the absolute error rather than the relative error because the estimated reference initial-spatial-distribution gradient is itself very small, with a magnitude on the order of 10^{-2}. Dividing by such a small reference gradient greatly amplifies Monte Carlo fluctuations and can produce large, statistically unstable relative errors even when the absolute difference between the two estimators is small. Although the absolute-error curve exhibits sampling fluctuations, its overall magnitude decreases as N increases, falling from approximately 1.32×10^{-1} at the smallest particle count to 6.03×10^{-3} at $N = 10^6$. This behavior indicates improving agreement between the adjoint and finite-difference sensitivities as the particle resolution is increased.

6.3. Two-sided inflow boundary conditions

Our third numerical example considers inflow boundary conditions at both ends of the spatial domain $\Omega = [0, 1]$. In contrast to the reflecting boundary conditions considered in the preceding examples, particles that leave the computational domain are removed, while new particles are introduced through both boundaries during every time step. Consequently, the number of active particles in the domain is not conserved.

The initial particle positions and velocities are sampled independently according to

$$X_{0,i} \sim \mathcal{U}([0,1]), \qquad V_{0,i} \sim \mathcal{N}(0, I_3), \qquad 1 \le i \le N_0,$$

where N_0 denotes the number of particles at the initial time. The inflow temperature vectors are

$$T_L = [4,4,4]^\top, \qquad T_R = [4,4,4]^\top.$$

Thus, both incoming distributions are isotropic and have the same temperature, but their components are treated as independent boundary parameters in the gradient computation.

At the left boundary, incoming particles satisfy $v^1 > 0$, whereas particles entering through the right boundary satisfy $v^1 < 0$. For a temperature vector $T = [T^1, T^2, T^3]^\top$, the incoming half-Maxwellian flux samples are generated as

$$v^1 = \sqrt{T^1}\sqrt{-2\log(1-U)} \quad \text{at } x = 0, \qquad v^1 = -\sqrt{T^1}\sqrt{-2\log(1-U)} \quad \text{at } x = 1,$$

and

$$v^2 = \sqrt{T^2}Z_2, \qquad v^3 = \sqrt{T^3}Z_3,$$

where $U \sim \mathcal{U}(0,1)$ and $Z_2, Z_3 \sim \mathcal{N}(0,1)$ are independent. Independently of the incoming velocity, we sample a residence time $\xi \sim \mathcal{U}([0, \Delta t])$. The positions of the injected particles at the end of the time step are therefore $x_L = v_L^1 \xi_L$ and $x_R = 1 + v_R^1 \xi_R$, where ξ_L and ξ_R are independent of their corresponding incoming velocities.

The computational inflow number density is set to $n_{\text{in}}^{(p)} = 1000 N_0$. At the boundary temperatures, the numbers of particles introduced during one time step are

$$N_L = \text{round}\left(\frac{\sqrt{T_L^1}}{\sqrt{2\pi}} \, \Delta x \, \Delta t \, n_{\text{in}}^{(p)} \right), \qquad N_R = \text{round}\left(\frac{\sqrt{T_R^1}}{\sqrt{2\pi}} \, \Delta x \, \Delta t \, n_{\text{in}}^{(p)} \right).$$

The values of N_L and N_R are evaluated at the given temperatures and then held fixed in both the ensemble-adjoint and finite-difference calculations.

The spatial and temporal discretizations are $\Delta x = 0.025$, $\Delta t = 0.025$, $M = 20$ and $T = M\Delta t = 0.5$. In each spatial cell Ω_j, the local particle count, density, and collision frequency are

$$N_k^j = |\mathcal{V}_k^j|, \qquad \rho_k^j = \frac{N_k^j}{N_0 |\Omega_j|}, \qquad \mu_k^j = \rho_k^j \int_{\mathbb{S}^2} q(\sigma) \, d\sigma.$$

The number of collision pairs is obtained by unbiased stochastic rounding of $N_k^j \Delta t \, \mu_k^j / 2$, and the collision particles are selected uniformly without replacement within the cell. In the numerical calculation, $\int_{\mathbb{S}^2} q(\sigma) \, d\sigma = 1$.

We consider $N_0 = 2 \times 10^6$. The injection counts are $N_L = N_R = 997{,}356$. The normalization used in the particle approximation of the objective is therefore $N_{\text{norm}} = N_0 + M(N_L + N_R) = 41{,}894{,}240$.

Figure 6 shows the macroscopic state generated by the two-sided inflow. The simulation starts with $N_0 = 2 \times 10^6$ particles and contains 32,033,761 active particles at $T = 0.5$. The normalized number density increases from its initial value $\widehat{n} \simeq 1$ to values between approximately 15.35 and 18.43. The final scalar temperature ranges from approximately 3.73 near the boundaries to 4.92 in the interior. The streamwise bulk velocity is positive near the left boundary and negative near the right boundary, reaching a magnitude of approximately 0.466, while its spatial mean remains close to zero. The approximate symmetry of the density and temperature profiles and the antisymmetry of the velocity profile are consistent with the equal left and right inflow temperatures and oppositely directed incoming fluxes.

For this experiment, we consider the localized kinetic-energy objective

$$J_3(T_L, T_R) = \int_0^1 \int_{\mathbb{R}^3} |v|^2 \exp\left[-36(x - 0.5)^2\right] f(x, v, T) \, dv \, dx. \tag{80}$$

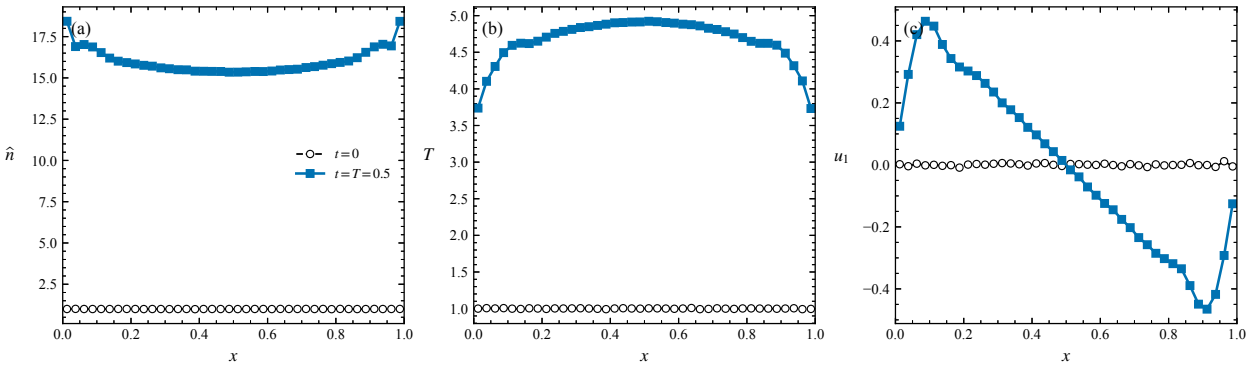


Figure 6: Two-sided inflow boundary conditions: profiles of (a) normalized number density $\widehat{n}$, (b) scalar temperature T, and (c) streamwise bulk velocity u_1 at $t = 0$ and $t = T = 0.5$. The simulation uses $N_0 = 2 \times 10^6$, $\Delta x = 0.025$, and the local-density-dependent collision frequency.

Its particle approximation is

$$\widehat{J}_3 = \frac{1}{N_{\text{norm}}} \sum_{i \in \mathcal{I}_M} |V_{M,i}|^2 \exp\left[-36(X_{M,i} - 0.5)^2\right],$$

where $\mathcal{I}_M$ denotes the particles that remain active at the terminal time. The Gaussian weight is centered at the midpoint of the domain and has the boundary value e^{-9}. Thus, the objective function measures kinetic energy transported through the interior and reduces the direct contribution from particles near the outflow boundaries.

We compute the gradient using the ensemble-adjoint formulation described in Section 5. The backward calculation propagates a scalar distributional adjoint through free transport and the adjoint of the locally linearized collision operator. The forward simulation uses the complete particle population to evaluate the exact cell counts and local collision frequencies, while a subset of the particle states is retained for the backward calculation. At every injection time, the boundary contribution is evaluated by multiplying the adjoint values at the sampled incoming states by the analytic temperature score of the half-Maxwellian flux distribution and summing over the source samples.

In this test, we focus on the two boundary-normal temperature derivatives

$$G_L = \frac{\partial J_3}{\partial T_L^1}, \qquad G_R = \frac{\partial J_3}{\partial T_R^1}.$$

These components control both the incoming normal-speed distribution and the distribution of the injected particle positions. The centered finite-difference approximations are

$$G_L^{\text{FD}} = \frac{J_3(T_L + he_1, T_R) - J_3(T_L - he_1, T_R)}{2h},$$

and

$$G_R^{\text{FD}} = \frac{J_3(T_L, T_R + he_1) - J_3(T_L, T_R - he_1)}{2h},$$

where $h = 0.025$. The values of N_L and N_R are retained in all perturbed forward calculations, and common random numbers are used within each centered finite-difference pair.

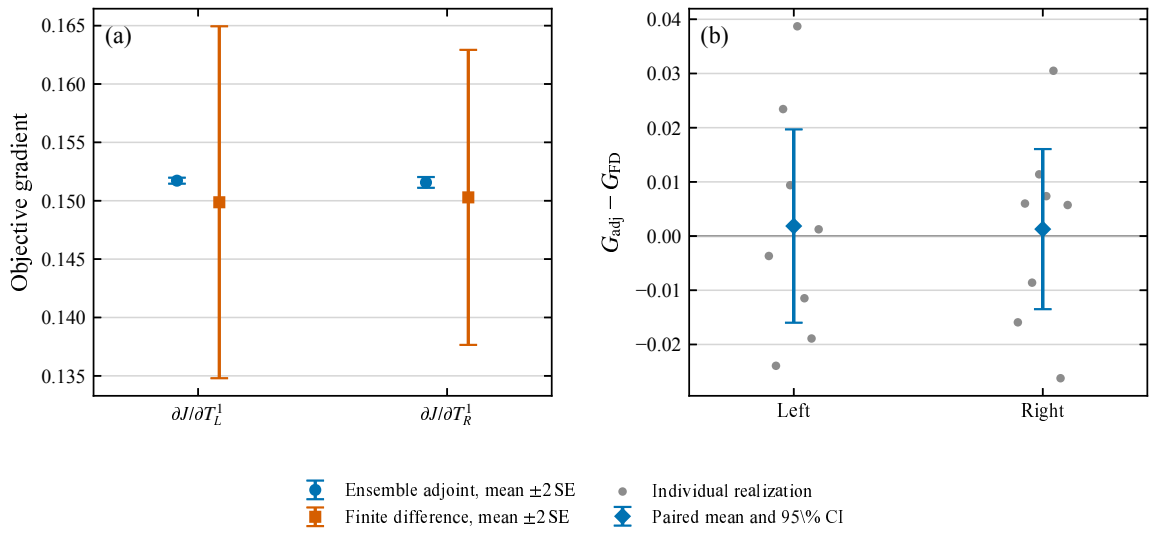


Figure 7: Ensemble-adjoint validation for the inflow boundary parameters. Each of the eight independently seeded realizations uses $N_0 = 2 \times 10^6$, finite-difference step $h = 0.025$, and 32,000 retained particles per cell. Panel (a) compares the ensemble-adjoint and finite-difference gradients; the error bars show two standard errors. Panel (b) shows the paired differences $G_{\mathrm{AJ}} - G_{\mathrm{FD}}$ for the individual realizations together with the paired mean and its 95% Student-t confidence interval. Both confidence intervals contain zero.

The validation uses eight independently seeded collision-and-inflow realizations, all sharing the same initial particle sample. Each realization uses $N_0 = 2 \times 10^6$, 32,000 retained particles per spatial cell, and 800,000 stored boundary-source samples per side. The ensemble-adjoint means and standard errors are

$$G_L^{\mathrm{AJ}} = 0.15171883 \pm 0.00012830, \qquad G_R^{\mathrm{AJ}} = 0.15157001 \pm 0.00023059,$$

whereas the corresponding finite-difference estimates are

$$G_L^{\mathrm{FD}} = 0.14986940 \pm 0.00753680, \qquad G_R^{\mathrm{FD}} = 0.15028809 \pm 0.00631838.$$

Here, each displayed uncertainty is one standard error across the eight realizations. The relative differences between the adjoint and finite-difference means are 1.23% and 0.85% at the left and right boundaries, respectively.

Figure 7(a) compares the two gradient estimators, with error bars showing twice the standard error. Panel (b) shows the realization-wise paired differences $G_{\mathrm{AJ}} - G_{\mathrm{FD}}$. Their 95% Student-$t$ confidence intervals are $[-0.01598, 0.01968]$ and $[-0.01349, 0.01605]$ at the left and right boundaries, respectively. Both intervals contain zero, so the observed mean discrepancies are not statistically significant at the 5% level. The substantially smaller error bars of the adjoint estimates also demonstrate that, for this calculation, the ensemble-adjoint estimator has much lower sampling variability than the centered finite difference.

We additionally examine the dependence of the adjoint estimates on the number of retained particles in each spatial cell. The results with 2,000, 8,000, and 32,000 retained particles per cell are shown in Figure 8. Increasing the number of retained particles moves both boundary-gradient estimates toward the eight-realization finite-difference means.

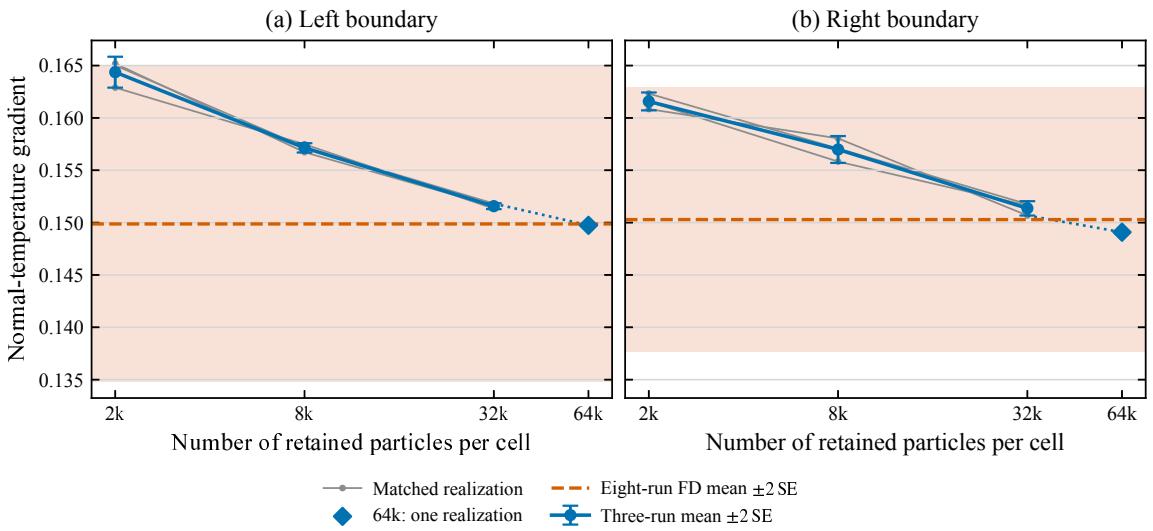


Figure 8: Convergence of the ensemble-adjoint gradients regarding (a) left and (b) right boundary-normal inflow temperatures with respect to the number of retained particles. The points through 32,000 retained particles per cell show the mean and two standard errors from three matched realizations; thin gray curves show the individual matched realizations. The 64,000-particle result is from one realization and is shown without a sampling error bar. The dashed line and shaded band denote the centered finite-difference mean and two standard errors from eight independently seeded realizations. The number of stored boundary-source samples is refined together with the number of retained particles.

A further calculation with 64,000 retained particles per cell and approximately 10^6 boundary-source samples per side continues this trend. This largest calculation contains only one realization, so it is shown without a sampling error bar.

6.4. High-Mach planar Couette flow

To examine the adjoint DSMC method in a regime where the sensitivity signal is large relative to the statistical fluctuations, we consider a planar Couette-flow problem with two oppositely moving thermal walls. As in the preceding examples, the spatial domain is $\Omega = [0, 1]$ and particles carry three-dimensional velocities. Both boundaries are modeled as diffuse thermal walls with the same isotropic temperature,

$$T_w = 1, \qquad T_L = T_R = T_w[1, 1, 1]^\top.$$

The walls move in opposite directions tangential to the spatial domain with the speed of:

$$U_L = [0, -U_w, 0]^\top, \qquad U_R = [0, U_w, 0]^\top, \qquad U_w = 4.$$

Taking the ratio of the wall speed to the equilibrium sound speed, with $\gamma = 5/3$, gives

$$\mathrm{Ma}_w = \frac{U_w}{\sqrt{\gamma T_w}} = \frac{4}{\sqrt{5/3}} \approx 3.10.$$

Thus, the prescribed boundary motion generates a high-Mach-number shear flow whose mean tangential velocity is substantially larger than the equilibrium velocity fluctuations.

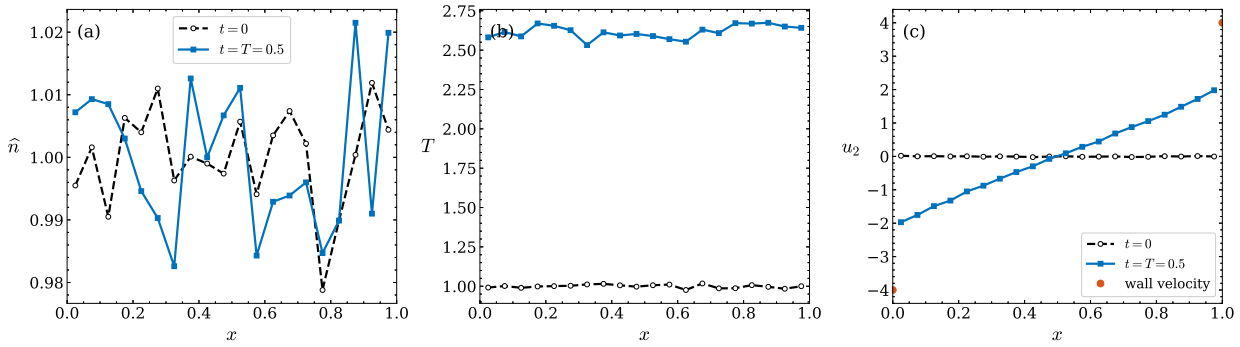


Figure 9: High-Mach Couette-flow macroscopic profiles computed with $N = 2\times10^5$, $\Delta x = 0.05$, and $T = 0.5$: (a) normalized number density, (b) scalar temperature, and (c) tangential bulk velocity. The black dashed and blue solid curves represent the profiles at $t = 0$ and $t = T$, respectively. The orange markers in panel (c) indicate the prescribed wall velocities $U_{L,2} = -4$ and $U_{R,2} = 4$.

For a particle diffusely re-emitted from the left wall, the velocity is sampled according to

$$V_1 = \sqrt{-2T_w \log(1-\xi_1)}, \qquad V_2 = -U_w + \sqrt{T_w}\,\xi_2, \qquad V_3 = \sqrt{T_w}\,\xi_3,$$

where $\xi_1 \sim \mathcal{U}(0,1)$ and $\xi_2, \xi_3 \sim \mathcal{N}(0,1)$. At the right wall, the sign of the normal velocity is reversed and the tangential mean velocity is $+U_w$:

$$V_1 = -\sqrt{-2T_w \log(1-\xi_1)}, \qquad V_2 = U_w + \sqrt{T_w}\,\xi_2, \qquad V_3 = \sqrt{T_w}\,\xi_3.$$

Consequently, the derivative of a re-emitted tangential velocity with respect to the wall-speed magnitude is -1 at the left wall and $+1$ at the right wall. The corresponding directional adjoint gradient is therefore

$$\frac{\partial J_4}{\partial U_w} = -\frac{\partial J_4}{\partial U_{L,2}} + \frac{\partial J_4}{\partial U_{R,2}}.$$

The gas is initially uniform in space and Maxwellian in velocity:

$$X_i(0) \sim \mathcal{U}([0,1]), \qquad V_i(0) \sim \mathcal{N}(0, I_3), \qquad 1 \le i \le N.$$

We use the spatial-cell width $\Delta x = 0.05$, the time-step size $\Delta t = 0.05$, and 10 time steps, giving a final time $T = 0.5$. For the adjoint calculation, the regularization width is $\varepsilon = \Delta t/10 = 0.005$. As in the preceding thermal-wall tests, the randomized time increment is used only for particles that may interact with a thermal wall during the current update.

Figure 9 shows the normalized number density, scalar temperature, and tangential bulk velocity at the initial and final times, computed using $N = 2 \times 10^5$ particles. The density remains approximately uniform, whereas viscous heating increases the gas temperature from its initial value of approximately 1 to approximately 2.62. More importantly, the initially vanishing tangential bulk velocity develops a clear, approximately linear shear profile. At the cell centers nearest the two walls, the final bulk velocities are approximately -1.98 and 1.99, respectively. The large and smoothly resolved velocity profile confirms that the macroscopic Couette signal is not obscured by thermal sampling noise.

To obtain a sensitivity with a comparably strong signal, we define the objective as the final mean tangential kinetic energy:

$$J_4(U_w) = \frac{1}{N}\sum_{i=1}^{N} V_{i,2}(T)^2.$$

This objective directly measures the kinetic energy generated by the moving walls. Its adjoint terminal condition is

$$\frac{\partial J_4}{\partial V_{i,2}(T)} = \frac{2V_{i,2}(T)}{N}, \qquad \frac{\partial J_4}{\partial X_i(T)} = 0.$$

Because U_w changes the two wall velocities in opposite directions, the contributions from the two boundaries add in $\partial J_4/\partial U_w$ rather than cancel.

We compare the adjoint gradient with the centered finite-difference approximation

$$\nabla^{\mathrm{FD}}_{U_w} J_4 = \frac{J_4(U_w+\delta) - J_4(U_w-\delta)}{2\delta}, \qquad \delta = 0.05.$$

The positive and negative perturbations use common random numbers. The finite-difference simulations employ the original deterministic time step, while the adjoint calculation uses the locally regularized boundary treatment. Thus, agreement between the two estimators is not produced by applying the same regularization to both calculations.

We vary the number of particles from $N = 10^3$ to $N = 2\times10^5$ and perform 96 independent realizations for every particle count. In addition to the relative difference between the mean gradients, we measure the statistical noise using the coefficient of variation

$$\mathrm{CV}(G) = \frac{\mathrm{std}(G)}{|\mathbb{E}[G]|}.$$

Unlike an absolute standard deviation, this quantity measures the fluctuations relative to the magnitude of the sensitivity signal and is therefore particularly suitable for assessing the noise level in this example.

The results are presented in Figure 10. The adjoint and finite-difference mean gradients are statistically compatible over the resolved range; their relative difference is below 2% for every $N \geq 2000$. At $N = 2 \times 10^5$, we obtain

$$\nabla^{\mathrm{AJ}}_{U_w} J_4 = 3.0283, \qquad \nabla^{\mathrm{FD}}_{U_w} J_4 = 3.0011,$$

corresponding to a relative difference of approximately 0.91%. At the same particle count, the coefficient of variation is approximately 1.87% for the adjoint estimator and 5.33% for the finite-difference estimator. Therefore, the sensitivity is resolved with relatively small statistical uncertainty, and the adjoint estimator is noticeably less noisy than the finite-difference benchmark.

This experiment complements the preceding near-equilibrium tests by examining a strongly driven flow with a clearly resolved macroscopic response. The agreement with the finite-difference benchmark demonstrates that the boundary adjoint remains accurate when the thermal walls possess large tangential velocities. Moreover, the small coefficient of variation shows that the observed agreement is not masked by statistical noise. The comparison also illustrates a practical advantage of the adjoint estimator: in the large-particle regime it has substantially smaller relative fluctuations than the centered finite-difference approximation.

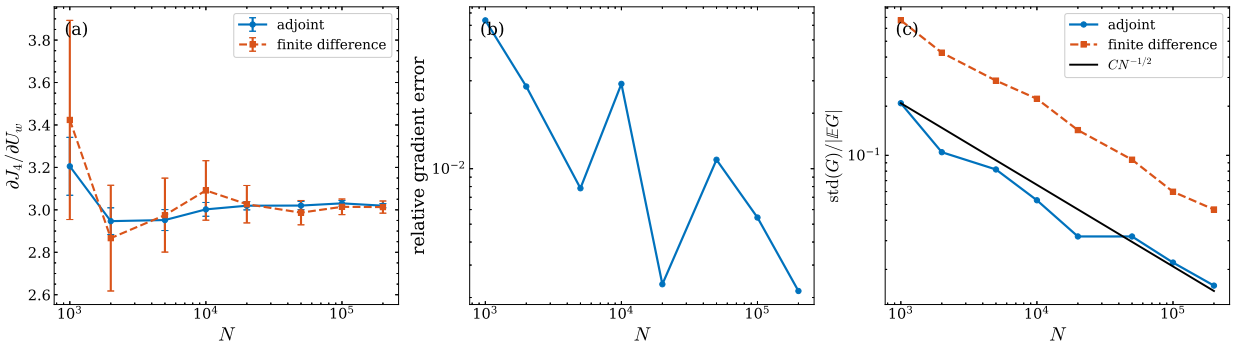


Figure 10: Adjoint-gradient validation for the high-Mach Couette-flow problem: (a) mean adjoint and finite-difference estimates of $\partial J_4/\partial U_w$, with error bars equal to twice the standard error of the mean; (b) relative difference between the mean adjoint and finite-difference gradients; and (c) coefficients of variation of the two gradient estimators. The black line in panel (c) shows an $N^{-1/2}$ reference rate. Results are based on 96 independent realizations for every particle count.

7. Discussions

This section discusses extensions to general collision kernels, the memory requirements of the adjoint formulations, the roles of objective selection and problem identifiability, and the treatment of objectives involving intermediate times.

7.1. Adjoint DSMC for a different collision kernel

The boundary adjoint relations derived in this work are associated with the transport and boundary maps, and therefore do not rely on the Maxwell-molecule collision model. If a more realistic molecular potential, such as hard spheres, is used, then the boundary part of the adjoint remains unchanged provided the same boundary reflection law is imposed. The collision part of the adjoint, however, must be replaced by the corresponding general-collision update, which includes the velocity-dependent collision rate and the associated score-function and adjoint Jacobian terms.

7.2. Memory consideration for Adjoint DSMC

The pathwise adjoint formulations for periodic, specular, and thermal boundary conditions require access to the realized forward trajectory. The particle states, collision pairings, boundary events, and sampled boundary variables may be either stored or reconstructed via checkpointing. Once this information is fixed, the corresponding backward sweep is deterministic.

The ensemble-adjoint inflow method has a different storage pattern. The forward calculation uses the complete active particle population, but the backward calculation stores only the exact cell counts, a prescribed subset of particle states in each cell, and samples of the boundary sources. The scalar adjoint field is reconstructed from these retained states, and its collision contribution is evaluated by Monte Carlo quadrature.

7.3. Gradient calculation versus optimization landscape

We emphasize that the adjoint DSMC method developed here provides gradients for a prescribed objective function; it does not by itself guarantee uniqueness of the associated

inverse problem. If the objective depends only on a moment of the final-time distribution, then different particle distributions, or different parameter values, may in principle produce the same objective value. As in many PDE-constrained optimization problems, uniqueness and convexity depend on the chosen parameterization, the available observations, and any regularization terms. Additional observables, time-integrated objectives, or regularization may be used to improve identifiability, but a general uniqueness theory is beyond the scope of this work.

7.4. Choice of the objective function

In the present work, the adjoint variables are not used to reweight the current particle cloud into an arbitrary target distribution. Instead, they propagate the sensitivity of a prescribed scalar objective with respect to the model or boundary parameters. For the moment-based objectives considered here, the target is a finite-dimensional quantity, not a full probability distribution, and therefore a support condition between two distributions is not required. If one wishes to formulate a full distribution-matching inverse problem, then the objective should be designed to avoid support mismatch, for example by using smooth observables, regularized discrepancies, time-integrated information, or continuation strategies.

7.5. Objectives involving intermediate times

For clarity, the preceding derivations use an objective depending only on the particle distribution at the final time. The same adjoint framework also applies to objectives involving the solution at intermediate times. For example, consider the time-integrated moment

$$\mathcal{J}_{\mathrm{int}}(m) = \int_0^T \int_\Omega \int_{\mathbb{R}^3} r(x,v,t) f(x,v,t;m)\,\mathrm{d}v\,\mathrm{d}x\,\mathrm{d}t. \tag{81}$$

Let $t_k = k\Delta t$, and let ω_k denote the weights of a temporal quadrature rule. For example, $\omega_k = \Delta t$, $0 \le k \le M-1$, and $\omega_M = 0$. A DSMC approximation of (81) is

$$\mathcal{J}_{\mathrm{int}}^N(m) = \frac{1}{N} \sum_{k=0}^{M} \omega_k \sum_{i \in \mathcal{I}_k} r(x_{k,i}, v_{k,i}, t_k), \tag{82}$$

where $\mathcal{I}_k$ denotes the set of particles present in the spatial domain at time t_k. For periodic, specular reflecting, and thermal BCs, $\mathcal{I}_k = \{1, \dots, N\}$. For inflow BC, the sum is restricted to particles that have entered the domain and have not yet exited.

For the pathwise formulations associated with periodic, specular, and thermal boundary conditions, the running objective produces source terms in the particle adjoints $\alpha_{k,i}$ and $\beta_{k,i}$, as described below. Here, $\widehat{\alpha}_{k,i}$ and $\widehat{\beta}_{k,i}$ denote, respectively, the position and velocity adjoint values obtained at time t_k by propagating the adjoints from later time levels backward through the collision, transport, and boundary updates, before adding the contribution of the running objective at t_k.

$$\alpha_{k,i} = \widehat{\alpha}_{k,i} - \omega_k \partial_x r(x_{k,i}, v_{k,i}, t_k), \tag{83}$$

$$\beta_{k,i} = \widehat{\beta}_{k,i} - \omega_k \partial_v r(x_{k,i}, v_{k,i}, t_k). \tag{84}$$

The terminal conditions become

$$\alpha_{M,i} = -\omega_M \partial_x r(x_{M,i}, v_{M,i}, t_M), \tag{85}$$

$$\beta_{M,i} = -\omega_M \partial_v r(x_{M,i}, v_{M,i}, t_M). \tag{86}$$

Thus, if $\omega_M = 0$, the terminal adjoint variables are zero, and the objective enters the adjoint system through the source terms in (83)-(84). The terminal-time objective considered in Sections 3, 4 and 5 is recovered by taking $\omega_M = 1$ and $\omega_k = 0$ for $k < M$.

For the ensemble-adjoint inflow formulation, the same principle is expressed at the distributional level. The derivative of the running observable enters as a source in the backward equation for $\lambda_k(x, v)$. Consequently, the adjoint value used in each local inflow-score contribution contains all subsequent running and terminal objective contributions.

For thermal boundary conditions, the same running source terms are added to the adjoint equations. In addition, the quantity multiplying a score-function term at time t_k must contain the portion of the objective affected by the randomized boundary transition at that time. Thus, the terminal objective r_i appearing in the thermal-boundary score-function terms in (49)-(50) need also be replaced.

Once the modified adjoint variables at the initial time have been computed, the gradient formulas retain the same form. Hence, incorporating observations at intermediate times does not require any change to the forward DSMC simulation and requires only additional source terms and, for thermal boundaries, a modification of the score term.

8. Conclusions

We have developed complementary adjoint DSMC formulations for the spatially inhomogeneous Boltzmann equation with periodic, specular reflecting, diffuse thermal, and prescribed inflow boundary conditions. Periodic and specular boundaries are treated using a pathwise particle adjoint conditional on the realized event history.

For diffuse thermal boundaries, a randomized-time regularization smooths the wall hit-or-miss event and permits its sensitivity to be represented by score-function terms. Reparameterized half-Maxwellian samples provide gradients with respect to wall temperatures and tangential wall velocities. For fixed ε, the method differentiates the regularized objective J_ε, which converges to the deterministic objective as $\varepsilon \to 0$. The numerical stability study indicates that the gradient is insensitive to ε over the range used in the experiments.

For prescribed inflow, we introduced an ensemble adjoint based on the locally linearized collision operator and a local likelihood-ratio score for the incoming boundary source. This construction accounts for the effect of perturbed incoming states on subsequent cell populations, local collision frequencies, and collision evolution. The present implementation conditions on fixed nominal injection counts; derivatives of a parameter-dependent physical injection intensity must be added separately.

Our results provide a practical, mathematically consistent adjoint framework for Boltzmann-constrained optimization and, more broadly, for particle-based adjoint methods for transport-dominated PDEs under realistic boundary conditions.

Our adjoint framework should naturally extend to more general stochastic reflection models, such as the Cercignani–Lampis boundary condition, provided the reflection law is

implemented via an explicit sampling procedure or a known conditional density for the post-reflection velocity of the form $p(v'|v, x)$.

A near-term direction of our work is the development and public release of a documented software package implementing the proposed adjoint DSMC framework.

Acknowledgment

Y. Y. was supported in part by the National Science Foundation under award DMS-2409855 and DMS-2540324 and by Office of Naval Research Grant under award N00014-24-1-2088. The authors thank Denis Silantyev for constructive discussions.

AI Disclosure Statement

During the preparation of this work, the authors used generative AI to improve readability and language tone. After using this tool, the authors reviewed and edited the content as needed and took full responsibility for the publication's content.

References

[1] Hans Babovsky and Reinhard Illner. A convergence proof for Nanbu's simulation method for the full Boltzmann equation. *SIAM Journal on Numerical Analysis*, 26(1):45–65, 1989.

[2] Hans Babovsky and H Neunzert. On a simulation scheme for the Boltzmann equation. *Mathematical Methods in the Applied Sciences*, 8(1):223–233, 1986.

[3] Guillaume Bal and Ian Langmore. Importance sampling and adjoint hybrid methods in Monte Carlo transport with reflecting boundaries. *arXiv preprint arXiv:1104.2550*, 2011.

[4] Atilim Gunes Baydin, Barak A Pearlmutter, Alexey Andreyevich Radul, and Jeffrey Mark Siskind. Automatic differentiation in machine learning: a survey. *Journal of machine learning research*, 18(153):1–43, 2018.

[5] Lorenz T Biegler, Omar Ghattas, Matthias Heinkenschloss, and Bart van Bloemen Waanders. Large-scale PDE-constrained optimization: an introduction. In *Large-Scale PDE-Constrained Optimization*, pages 3–13. Springer, 2003.

[6] GA Bird. Direct simulation and the Boltzmann equation. *The Physics of Fluids*, 13(11):2676–2681, 1970.

[7] Graeme A Bird. Molecular gas dynamics and the direct simulation of gas flows. *Molecular gas dynamics and the direct simulation of gas flows*, 1994.

[8] Russel Caflisch, Denis Silantyev, and Yunan Yang. Adjoint DSMC for nonlinear Boltzmann equation constrained optimization. *Journal of Computational Physics*, 439:110404, 2021.

[9] Russel Caflisch and Yunan Yang. Adjoint Monte Carlo Method. *Active Particles, Volume 4: Theory, Models, Applications*, pages 461–505, 2024.

[10] Carlo Cercignani. The Boltzmann equation and its applications. 1988. *Applied Mathematical Sciences*, 1988.

[11] Carlo Cercignani. *Rarefied gas dynamics: from basic concepts to actual calculations*, volume 21. Cambridge University Press, 2000.

[12] Andreas Griewank and Andrea Walther. *Evaluating derivatives: principles and techniques of algorithmic differentiation*. SIAM, 2008.

[13] Kaiwen Guan and Takayuki Yamada. Topology optimization of rarefied gas flows using an adjoint discrete velocity method. *Journal of Computational Physics*, 511:113111, 2024.

[14] Michael Hinze, René Pinnau, Michael Ulbrich, and Stefan Ulbrich. *Optimization with PDE constraints*, volume 23. Springer Science & Business Media, 2008.

[15] Jan Eduard Hoogenboom. *Adjoint Monte Carlo methods in neutron transport calculations*. PhD thesis, Delft University Press, 1977.

[16] Qin Li, Li Wang, and Yunan Yang. Monte Carlo Gradient in Optimization Constrained by Radiative Transport Equation. *SIAM Journal on Numerical Analysis*, 61(6):2744–2774, 2023.

[17] Emil Løvbak, Frédéric Blondeel, Adam Lee, Lander Vanroye, Andreas Van Barel, and Giovanni Samaey. Reversible random number generation for adjoint Monte Carlo simulation of the heat equation. In *International Conference on Monte Carlo and Quasi-Monte Carlo Methods in Scientific Computing*, pages 451–468. Springer, 2022.

[18] Shakir Mohamed, Mihaela Rosca, Michael Figurnov, and Andriy Mnih. Monte Carlo gradient estimation in machine learning. *Journal of Machine Learning Research*, 21(132):1–62, 2020.

[19] Kenichi Nanbu. Direct simulation scheme derived from the Boltzmann equation. I. monocomponent gases. *Journal of the Physical Society of Japan*, 49(5):2042–2049, 1980.

[20] Angxiu Ni. Ergodic and foliated kernel-differentiation method for linear responses of random systems. *Journal of Nonlinear Science*, 35(5):90, 2025.

[21] Lorenzo Pareschi and Giovanni Russo. An introduction to Monte Carlo method for the Boltzmann equation. In *ESAIM: Proceedings*, volume 10, pages 35–75. EDP Sciences, 2001.

[22] Reuven Y Rubinstein. The score function approach for sensitivity analysis of computer simulation models. *Mathematics and Computers in Simulation*, 28(5):351–379, 1986.

[23] Facundo Sapienza, Jordi Bolibar, Frank Schäfer, Brian Groenke, Avik Pal, Victor Boussange, Patrick Heimbach, Giles Hooker, Fernando Pérez, Per-Olof Persson, et al. Differentiable programming for differential equations: A review. *arXiv preprint arXiv:2406.09699*, 2024.

[24] Ting Wang and Muruhan Rathinam. Efficiency of the Girsanov transformation approach for parametric sensitivity analysis of stochastic chemical kinetics. *SIAM/ASA Journal on Uncertainty Quantification*, 4(1):1288–1322, 2016.

[25] Yunan Yang, Denis Silantyev, and Russel Caflisch. Adjoint DSMC for nonlinear spatially-homogeneous Boltzmann equation with a general collision model. *Journal of Computational Physics*, page 112247, 2023.

[26] Ruifeng Yuan and Lei Wu. A design optimization method for rarefied and continuum gas flows. *Journal of Computational Physics*, 517:113366, 2024.

[27] Ruifeng Yuan and Lei Wu. Adjoint shape optimization from the continuum to free-molecular gas flows. *Journal of Computational Physics*, page 114102, 2025.

Appendix A. Formula of $\partial_x \log p_l(x,v)$ and $\partial_v \log p_l(x,v)$ in Section 4.2.4

This appendix provides detailed calculations of the score-function terms introduced in Section 4.2.4 for the adjoint system associated with the thermal boundary condition.

For the 1D domain $\Omega = [L, R]$, define

$$t_i^L = \frac{L - x_{k,i}}{\mathcal{P}v'_{k,i}}, \qquad t_i^R = \frac{R - x_{k,i}}{\mathcal{P}v'_{k,i}}.$$

If $\mathcal{P}v'_{k,i} < 0$, then

$$(p_1, p_2, p_3) = \big(1 - F_{\Delta t,\varepsilon}(t_i^L),\ F_{\Delta t,\varepsilon}(t_i^L),\ 0\big),$$

while if $\mathcal{P}v'_{k,i} > 0$, then

$$(p_1, p_2, p_3) = \big(0,\ F_{\Delta t,\varepsilon}(t_i^R),\ 1 - F_{\Delta t,\varepsilon}(t_i^R)\big),$$

where $F_{\Delta t,\varepsilon}$ denotes the cumulative distribution function of $\mathcal{N}(\Delta t, \varepsilon^2)$. We also denote by $f_{\Delta t,\varepsilon}$ its probability density function. Here, p_l is a short-hand notation for $p_l(x,v)$, $l = 1, 2, 3$.

Define the hazard and reverse-hazard ratios

$$\lambda(t) := \frac{f_{\Delta t,\varepsilon}(t)}{F_{\Delta t,\varepsilon}(t)}, \qquad \bar{\lambda}(t) := \frac{f_{\Delta t,\varepsilon}(t)}{1 - F_{\Delta t,\varepsilon}(t)}.$$

For $\mathcal{P}v < 0$ set $t^L = \frac{L-x}{\mathcal{P}v}$, and for $\mathcal{P}v > 0$ set $t^R = \frac{R-x}{\mathcal{P}v}$. Then

$$\begin{aligned}
\nabla_x \log p_1(x,v) &= \mathbb{1}_{\mathcal{P}v<0}\, \frac{1}{\mathcal{P}v}\, \bar{\lambda}(t^L), \\
\nabla_x \log p_2(x,v) &= -\mathbb{1}_{\mathcal{P}v<0}\, \frac{1}{\mathcal{P}v}\, \lambda(t^L) - \mathbb{1}_{\mathcal{P}v>0}\, \frac{1}{\mathcal{P}v}\, \lambda(t^R), \\
\nabla_x \log p_3(x,v) &= \mathbb{1}_{\mathcal{P}v>0}\, \frac{1}{\mathcal{P}v}\, \bar{\lambda}(t^R),
\end{aligned}$$

and

$$\nabla_v \log p_1(x,v) = \mathbb{1}_{\mathcal{P}v<0}\,\frac{t^L}{\mathcal{P}v}\,\bar{\lambda}(t^L)\,\mathcal{P}^*,$$
$$\nabla_v \log p_2(x,v) = -\mathbb{1}_{\mathcal{P}v<0}\,\frac{t^L}{\mathcal{P}v}\,\lambda(t^L)\,\mathcal{P}^* - \mathbb{1}_{\mathcal{P}v>0}\,\frac{t^R}{\mathcal{P}v}\,\lambda(t^R)\,\mathcal{P}^*,$$
$$\nabla_v \log p_3(x,v) = \mathbb{1}_{\mathcal{P}v>0}\,\frac{t^R}{\mathcal{P}v}\,\bar{\lambda}(t^R)\,\mathcal{P}^*.$$